

Sensitive fluorescent biosensor reveals differential subcellular regulation of PKC

Received: 9 November 2023

Accepted: 20 September 2024

Published online: 11 October 2024

 Check for updates

Qi Su¹, Jing Zhang^{1,2,7}, Wei Lin^{1,7}, Jin-Fan Zhang^{3,6}, Alexandra C. Newton^{1,2},
Sohum Mehta¹, Jing Yang^{1,2,4} & Jin Zhang^{1,2,3,5} ✉

The protein kinase C (PKC) family of serine and threonine kinases, consisting of three distinctly regulated subfamilies, has been established as critical for various cellular functions. However, how PKC enzymes are regulated at different subcellular locations, particularly at emerging signaling hubs, is unclear. Here we present a sensitive excitation ratiometric C kinase activity reporter (ExRai-CKAR2) that enables the detection of minute changes (equivalent to 0.2% of maximum stimulation) in subcellular PKC activity. Using ExRai-CKAR2 with an enhanced diacylglycerol (DAG) biosensor, we uncover that G-protein-coupled receptor stimulation triggers sustained PKC activity at the endoplasmic reticulum and lysosomes, differentially mediated by Ca²⁺-sensitive conventional PKC and DAG-sensitive novel PKC, respectively. The high sensitivity of ExRai-CKAR2, targeted to either the cytosol or partitioning defective complexes, further enabled us to detect previously inaccessible endogenous atypical PKC activity in three-dimensional organoids. Taken together, ExRai-CKAR2 is a powerful tool for interrogating PKC regulation in response to physiological stimuli.

The protein kinase C (PKC) family of enzymes has critical roles in regulating myriad cellular processes, including cell growth, differentiation and death. Aberrant PKC signaling drives many diseases, such as cancer, diabetes and neurodegeneration^{1–4}. Loss-of-function (LOF) PKC mutations^{1,2}, including LOF fusion oncoproteins⁵, are frequently associated with cancer. Various PKC isoforms also have critical roles in synaptic plasticity, with isoform-selective knockout mice showing major neurological deficits^{6,7}. On the other hand, elevated PKC α activity is linked to impaired cognitive function in an Alzheimer's disease mouse model⁴. Thus, cells must be able to precisely balance PKC activity levels, as either too little or too much PKC activity can trigger pathological states. Targeting specific PKC isoforms and their aberrant functions could, thus, unlock new therapeutic directions⁸.

The nine PKC isoforms comprise three families: conventional PKC (cPKC), novel PKC (nPKC) and atypical PKC (aPKC). cPKC isoforms are activated by the binding of both Ca²⁺ and diacylglycerol (DAG),

whereas nPKCs are activated by DAG alone, as their C2 domains lack Ca²⁺-coordinating residues, while their C1 domains exhibit higher DAG affinity⁹. aPKCs show the greatest divergence, not only lacking functional C1 domains but also substituting their C2 domains for PBI domains that mediate interactions with specific scaffold proteins to induce kinase activation¹⁰. In cells, PKC activity is tightly regulated at different subcellular locations through the interplay of second messengers, scaffold proteins, upstream kinases and phosphatases. In the traditional model, activation of G α_q -protein-coupled receptors induces plasma membrane (PM) phospholipase C (PLC) activity, triggering the production of DAG and inositol trisphosphate, the latter of which further evokes Ca²⁺ release from the endoplasmic reticulum (ER). Binding of Ca²⁺ and/or DAG recruits both cPKCs and nPKCs to the PM, the strongest site of cPKC activation^{11–14}. However, emerging evidence suggests that PKCs are active at other subcellular locations, such as the Golgi¹¹ and nucleus¹⁵, and that PKCs can impact biological functions at other

¹Department of Pharmacology, University of California San Diego, La Jolla, CA, USA. ²Moore's Cancer Center, University of California San Diego, La Jolla, CA, USA. ³Shu Chien-Gene Lay Department of Bioengineering, University of California San Diego, La Jolla, CA, USA. ⁴Department of Pediatrics, University of California San Diego, La Jolla, CA, USA. ⁵Department of Chemistry and Biochemistry, University of California San Diego, La Jolla, CA, USA. ⁶Present address: Department of Chemistry and Chemical Biology, Harvard University, Cambridge, MA, USA. ⁷These authors contributed equally: Jing Zhang, Wei Lin. ✉e-mail: jzhang32@health.ucsd.edu

subcellular organelles. For instance, ER stress^{16,17} and the accumulation of lipids at the ER were each shown to activate PKC¹⁸. PKC is also implicated in lysosome biogenesis^{19,20}. Yet, it remains unclear how PKCs are regulated at the ER or lysosome. aPKCs are also essential in regulating epithelial cell polarity and tumor epithelial–mesenchymal transition (EMT)^{21,22}. The partitioning defective 3 (Par3)–Par6–aPKC complex promotes tight junction and apical domain formation by phosphorylating and excluding various targets from the apical domain^{22–24}. However, the activity dynamics and regulation of aPKC at Par complexes during polarity formation remain elusive, especially in three-dimensional (3D) cultures, hindered by a lack of appropriate tools^{10,22,25}.

Genetically encoded fluorescent biosensors are powerful tools to monitor kinase activities and small-molecule dynamics, among various cellular events, *in situ*. Such biosensors have previously been used to study PKC activity in living cells, understand kinase structure–function relationships and interrogate PKC regulation in various diseases^{26,27}. The first Förster resonance energy transfer (FRET)-based C kinase activity reporter (CKAR) was developed about two decades ago, comprising a PKC-specific substrate peptide and phosphoamino acid-binding FHA2 domain as the sensing unit sandwiched between a cyan fluorescent protein (CFP) and yellow fluorescent protein (YFP) FRET pair²⁸. CKAR has provided numerous insights into the regulation of PKC isoforms at different subcellular organelles. For example, Golgi-localized CKAR revealed sustained PKC activity by Ca²⁺-induced DAG synthesis at the Golgi¹¹. Similarly, isoform-specific CKARs illuminated several long-overlooked aspects of PKC isoform regulation, such as Src kinase-controlled nuclear PKC δ activity¹⁵ and agonist-evoked aPKC activity^{25,29}. However, FRET-based biosensors are limited by their small dynamic ranges^{15,25}, whereby minute activities, such as that of endogenous aPKC in 3D cultures, have remained beyond the reach of these tools¹⁰.

Building on a recently developed excitation ratiometric (ExRai) KAR design^{30–32}, we report a second-generation ExRai PKC activity reporter (ExRai-CKAR2) that enables highly sensitive tracking of PKC activity dynamics in living cells. We demonstrate the sensitivity and utility of ExRai-CKAR2 by elucidating the regulation of PKC isoforms at the ER and lysosome and by measuring endogenous, basal aPKC activity in polarized Madin–Darby canine kidney (MDCK) organoids and lumenogenesis-related aPKC activity at the Par complex in HEK293T organoids. Our results highlight the versatility of this robust biosensor in deciphering the spatiotemporal regulation of PKC in highly physiologically relevant settings.

Results

Development and characterization of ExRai-CKAR2

Our ExRai-KAR series consists of circularly permuted enhanced green fluorescent protein (cpEGFP) sandwiched between a kinase-specific substrate peptide and phosphoamino acid-binding FHA1 domain. ExRai-KARs exhibit two excitation peaks, one at ~400 nm and another at ~509 nm, with a distinct shoulder at ~480 nm, corresponding to the neutral and anionic states of the GFP chromophore³³, and a single emission peak at ~515 nm (ref. 34). Phosphorylation of the substrate peptide by the target kinase triggers binding by the FHA1 domain, leading to a conformational change that increases fluorescence emission by the anionic species (for example, 480-nm excitation) and decreases fluorescence emission by the neutral species (for example, 400-nm excitation) (Fig. 1a). The ratio of fluorescence intensity at these two excitation wavelengths (that is, the 480/400 excitation ratio) serves as a readout of kinase activity. Previously, we succeeded in generating an ExRai PKC sensor, ExRai-CKAR, by incorporating an established PKC-specific substrate peptide into this design³⁴. To improve ExRai-CKAR performance, we took advantage of our recent success optimizing ExRai-KARs^{30–32} and substituted the two residues immediately preceding and following cpEGFP in ExRai-CKAR. We tested several linker variants in HeLa cells stimulated with phorbol 12-myristate 13-acetate (PMA) to identify a

sensor with an increased PKC-stimulated change in excitation ratio (Supplementary Fig. 1a). Of the biosensors tested, the variant with the linker pair SY–IS showed the largest response (Supplementary Fig. 1b) and was designated ExRai-CKAR2 (Fig. 1a).

As expected, purified ExRai-CKAR2 protein displayed two excitation maxima at approximately 400 nm and 500 nm *in vitro*, with a single emission peak at 516 nm (Fig. 1b). *In vitro* phosphorylation by PKC α in the presence of adenosine triphosphate (ATP) decreased the intensity at 405-nm excitation by 38% and increased the intensity at 480-nm excitation by 328% versus conditions of no ATP and no Ca²⁺, resulting in a 333% \pm 9% (Supplementary Table 1) increase in the 480/405 excitation ratio ($(R_+ - R_-)/R_-$).

In Cos7 cells, ExRai-CKAR2 showed a 289% \pm 12% increase in the 480/405 excitation ratio ($\Delta R/R_0$, mean \pm s.e.m., $n = 35$ cells) upon PMA stimulation (Fig. 1c–e), a significant enhancement versus both the 46% \pm 5% emission ratio change from the second-generation FRET-based sensor CKAR2 ($n = 20$)³⁵ and the 72% \pm 1% ($n = 27$) change in excitation ratio from ExRai-CKAR1 (ref. 34) (Fig. 1e,f). The slightly reduced amplitude versus the *in vitro* response might be because of intracellular phosphatase activity²⁸. Indeed, treating cells with calyculin A to suppress phosphatase activity following PMA stimulation increased the ExRai-CKAR2 response to 429% \pm 18% ($\Delta R/R_0$, $n = 26$; Supplementary Fig. 2). The addition of Gö6983, a potent pan-PKC inhibitor, reversed the PMA-induced responses to the baseline level (Fig. 1c,d), confirming the reversibility of the sensor. Meanwhile, a nonphosphorylatable mutant sensor (ExRai-CKAR2 T/A) showed no response in Cos7 cells treated with PMA and Gö6983 (Fig. 1c,d and Supplementary Fig. 3). ExRai-CKAR2 also did not respond to activation of other AGC family kinases, as neither activation of PKA using forskolin and 3-isobutyl-1-methylxanthine nor stimulation of Akt activity using platelet-derived growth factor in the presence of the PKC inhibitor Gö6983 evoked a detectable ExRai-CKAR2 ratio change (Supplementary Fig. 4a,b)^{28,30,31}. Stimulating extracellular signal-regulated kinase (ERK) activity using epidermal growth factor or adenosine monophosphate-activated kinase activity using 2-deoxyglucose similarly failed to evoke detectable ExRai-CKAR2 responses (Supplementary Fig. 4c,d), confirming that ExRai-CKAR2 specifically reports PKC activity. Compared to CKAR2 and ExRai-CKAR1, ExRai-CKAR2 showed a broader PMA dose–response curve (Supplementary Fig. 5), responding to PMA doses as low as 0.1 ng ml⁻¹ (equivalent to 0.2% maximum stimulation) at endogenous PKC expression levels in Cos7 cells with a 2.8% \pm 0.5% ratio change ($n = 33$), whereas ExRai-CKAR1 and CKAR2 only started responding at doses above 0.5 and 5 ng ml⁻¹, respectively (Supplementary Fig. 5), suggesting 5–50-fold higher sensitivity with ExRai-CKAR2. The improved sensitivity and broad response curve allowed us to detect both subtle and strong PKC activities. Overall, ExRai-CKAR2 exhibited high selectivity, sensitivity and dynamic range.

Sensitive detection of compartmentalized PKC activity

PKC is present not only at the PM but also at various subcellular locations. Yet, the regulation of different PKC isoforms at several emerging subcellular locations is not well understood. To enable sensitive detection of subcellular PKC activity, we targeted ExRai-CKAR2 to specific subcellular regions using established targeting motifs (Fig. 2 and Supplementary Fig. 6): a nuclear export signal (NES) for cytosolic targeting (Cyto-ExRai-CKAR2), a lipid modification motif derived from Lyn kinase (Lyn) for PM targeting (PM-ExRai-CKAR2), a cytochrome P450 (CYP450)-derived sequence for ER targeting (ER-ExRai-CKAR2) and a domain derived from full-length lysosome-associated membrane protein 1 (LAMP1) for lysosomal targeting³¹ (Lyso-ExRai-CKAR2).

Upon PMA stimulation, Cyto-ExRai-CKAR2 and PM-ExRai-CKAR2 reported 290% \pm 15% (Fig. 2a; $n = 27$) and 144% \pm 16% (Fig. 2b; $n = 27$) increases in the 480/405 excitation ratio in the cytosol and at the PM, respectively, consistent with well-characterized PKC activity at these locations. Conversely, no response was detected using ExRai-CKAR2

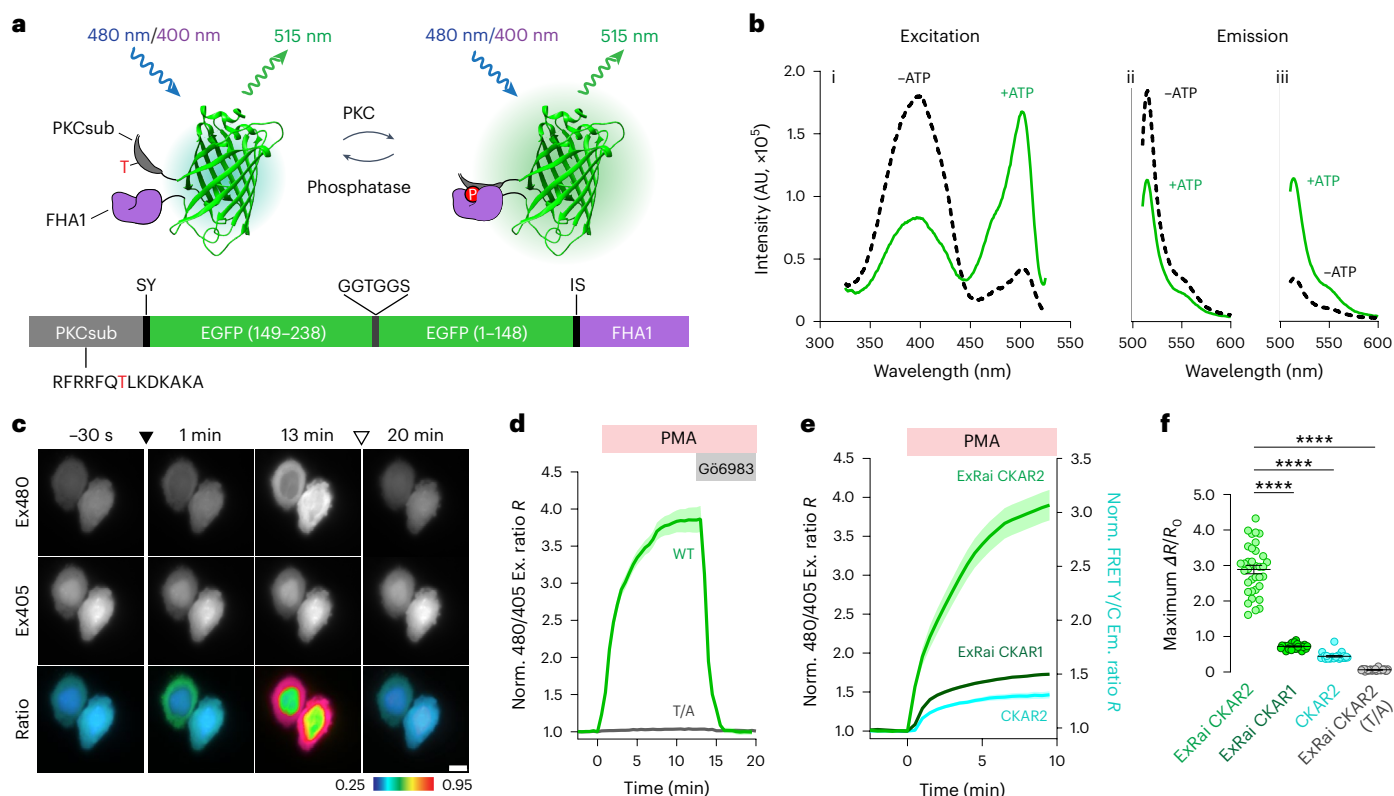


Fig. 1 | Development and characterization of ExRai-CKAR2. **a**, Top, modulation of cpEGFP fluorescence by a molecular switch dependent on PKC-mediated phosphorylation. Bottom, domain structure of ExRai-CKAR2. **b**, Representative in vitro ExRai-CKAR2 fluorescence spectra collected at 530-nm emission (i) and 405-nm (ii) or 480-nm excitation (iii) without (black traces) or with (green traces) ATP, Ca^{2+} and lipids in the presence of purified PKC α ($n = 3$ independent experiments). AU, arbitrary units. **c**, Representative images of ExRai-CKAR2 fluorescence in Cos7 cells at 480-nm (Ex480, top) and 405-nm (Ex405, middle) excitation. Bottom, pseudocolored images of the change in excitation ratio upon PMA stimulation and G66983 inhibition. Warmer colors indicate higher ratios. The solid arrowhead indicates PMA addition and the hollow arrowhead indicates G66983 addition. Images are representative of three independent

experiments. Scale bar, 10 μm . **d**, Representative average time courses showing the 480/405 excitation ratio responses of wild-type (WT) ExRai-CKAR2 and a nonphosphorylatable ExRai-CKAR2 T/A mutant in Cos7 cells treated with PMA and G66983. **e**, Representative average time courses comparing the 480/405 excitation ratio or Y/C emission ratio responses of ExRai-CKAR2, ExRai-CKAR1 or CKAR2 in Cos7 cells treated with 50 ng ml^{-1} PMA. **f**, Quantification of the maximum PMA-stimulated response of each biosensor ($n = 35$, $n = 27$, $n = 20$ and $n = 22$ cells from three independent experiments each). Time courses in **d**, **e** are representative of three independent experiments; solid lines indicate mean responses and shaded areas indicate the s.e.m. Data in **f** were analyzed using ordinary one-way ANOVA followed by Dunnett's multiple-comparison test. **** $P < 0.0001$. Data are the mean \pm s.e.m.

T/A targeted to either location (Fig. 2a,b). ER-ExRai-CKAR2 and Lyso-ExRai-CKAR2 also revealed PMA-induced PKC activity at the ER and lysosome membranes, two previously underappreciated sites of PKC signaling. ER-ExRai-CKAR2 responded to PMA stimulation with a $234\% \pm 22\%$ ($n = 39$) increase in the 480/405 excitation ratio, whereas the T/A mutant showed no PMA-induced response (Fig. 2c). Similarly, Lyso-ExRai-CKAR2 exhibited a $178\% \pm 12\%$ increase in excitation ratio upon PMA stimulation ($n = 33$), whereas no response was detected using the T/A mutant sensor (Fig. 2d). In summary, ExRai-CKAR2 enables sensitive and robust detection of PKC activity at various subcellular locations.

PKC regulation at the ER and lysosome

Although traditionally regarded as organelles dedicated to overseeing protein trafficking, quality control and degradation, the ER and lysosome have emerged as key intracellular signaling hubs^{36–38}. The ER and lysosomal PKC activities detected using targeted ExRai-CKAR2 are consistent with past reports that PKC α accumulates on the ER surface upon phorbol ester activation in 3T3 cells³⁹ and that PKC contributes to lysosome biogenesis, with PMA stimulation inducing PKC localization to lysosomes¹⁹. However, the regulation of PKC activity at these sites in response to physiological signals has not been explored. We, therefore, set out to investigate ER and lysosomal PKC regulation in response to

uridine triphosphate (UTP) stimulation of the $\text{G}\alpha_q$ -protein-coupled P2Y receptor.

As shown in Fig. 3a, UTP stimulation of ER-ExRai-CKAR2-expressing or Lyso-ExRai-CKAR2-expressing Cos7 cells induced clear elevations in PKC activity, with a $21\% \pm 2\%$ increase in excitation ratio from ER-ExRai-CKAR2 ($n = 36$) and a $40\% \pm 2\%$ increase in excitation ratio from Lyso-ExRai-CKAR2 ($n = 36$). We next assessed the dynamics of agonist-induced PKC activity at these two locations by quantifying the fractional sensor response remaining 15 min after stimulation versus the maximum response (that is, sustained activity metric at 15 min (SAM15))^{40,41}. Interestingly, UTP induced sustained PKC activity at both locations, with SAM15 values of 0.65 ± 0.02 at the ER and 0.92 ± 0.05 at the lysosome (Fig. 3a). By contrast, UTP stimulation induced a sharp $75\% \pm 3\%$ ($n = 25$) increase in excitation ratio from PM-ExRai-CKAR2, which quickly reversed, showing a SAM15 value of 0.06 ± 0.05 (Fig. 3a), consistent with previous findings that $\text{G}\alpha_q$ signaling mediates rapid, transient PKC activity at the PM¹¹. Notably, treatment with the pan-PKC inhibitor G66983 following UTP stimulation only partly reversed the ER-ExRai-CKAR2 response compared to Lyso-ExRai-CKAR2 (Supplementary Fig. 7a,b). This effect was recapitulated using FRET-based ER-CKAR2 (Supplementary Fig. 7c) and was rescued in cells overexpressing protein phosphatase 2A (Supplementary Fig. 7d), suggesting that a lower level of phosphatase activity at the ER was responsible.

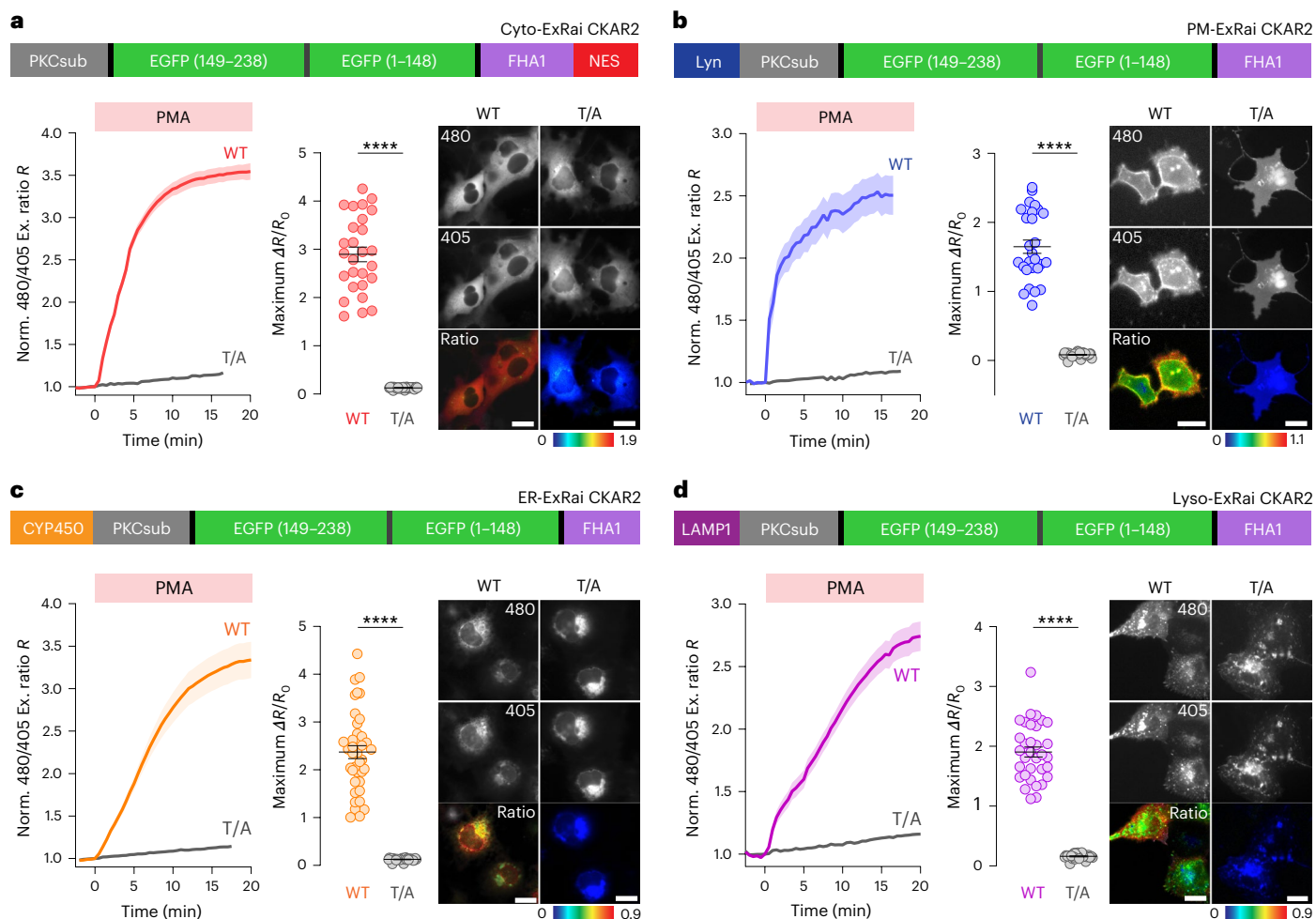


Fig. 2 | Subcellular targeting of ExRai-CKAR2. **a–d**, Domain structures (top), average 480/405 excitation ratio time courses (bottom left), quantification of maximum response (bottom middle) and representative images (bottom right) of ExRai-CKAR2 and ExRai-CKAR2 T/A negative control targeted to the cytoplasm (**a**; WT, $n = 27$ cells; T/A, $n = 30$ cells), PM (**b**; WT, $n = 27$ cells; T/A, $n = 30$ cells), ER (**c**; WT, $n = 39$ cells; T/A, $n = 30$ cells) and lysosomes (**d**, WT, $n = 33$ cells;

T/A, $n = 30$ cells) in Cos7 cells stimulated with 50 ng ml^{-1} PMA. Scale bars, $10 \mu\text{m}$. Time courses are representative of three independent experiments; solid lines indicate mean responses and shaded areas indicate the s.e.m. Statistical analyses were performed using a two-sided Student's t -test. **** $P < 0.0001$. Data are the mean \pm s.e.m.

We then investigated the contribution of different PKC isoforms to these ER and lysosome PKC activity signatures. Pretreating Cos7 cells with $1 \mu\text{M}$ Gö6976, a cPKC-specific inhibitor, before UTP addition greatly reduced the response from ER-ExRai-CKAR2 to $4.7\% \pm 0.4\%$ (Fig. 3b,d; $n = 34$), suggesting that cPKC accounts for roughly three quarters of the receptor-mediated ER PKC response. Conversely, an nPKC inhibitor, B106, showed no effect on UTP-stimulated ER PKC activity (Fig. 3c,d). PKC α and PKC β are the two cPKC isoforms present in Cos7 cells^{42–44}. Small interfering RNA (siRNA) knockdown of individual isoforms revealed PKC α as the dominant ER isoform, as PKC α knockdown suppressed roughly 84% of the UTP-stimulated ER-ExRai-CKAR2 response, which dropped to $3.4\% \pm 0.3\%$ (Fig. 3e; $n = 24$), whereas PKC β knockdown decreased the response by only 60% to $9\% \pm 1\%$ (Fig. 3e and Supplementary Fig. 8; $n = 19$). Moreover, overexpressing PKC α increased the UTP-stimulated ER-ExRai-CKAR2 response to $39\% \pm 3\%$ (Fig. 3b,d; $n = 32$). Consistent with these observations, we found that Ca²⁺ was essential but not sufficient for ER PKC activity (Supplementary Fig. 9), as cPKC activation requires both Ca²⁺ and DAG.

In contrast, Gö6976 pretreatment had no effect on the maximum UTP-stimulated Lyso-ExRai-CKAR2 response, yielding a $43\% \pm 2\%$ change in ratio similar to control cells (Fig. 3f,h; $n = 37$). Instead, pretreatment with $5 \mu\text{M}$ B106, an nPKC-specific inhibitor designed for

PKC δ (ref. 45), significantly decreased the UTP-induced lysosomal PKC activity reported by Lyso-ExRai-CKAR2 to $10.1\% \pm 0.8\%$ (Fig. 3g,h; $n = 24$), suggesting a more critical role for nPKC in controlling PKC activity at the lysosome. Consistently, siRNA knockdown of PKC δ significantly decreased the UTP-stimulated Lyso-ExRai-CKAR2 response to $7\% \pm 1\%$ (Fig. 3i and Supplementary Fig. 10; $n = 19$), whereas overexpressing PKC δ strongly increased the UTP-stimulated response from Lyso-ExRai-CKAR2 to $61\% \pm 3\%$ (Fig. 3g,h; $n = 28$). These results suggest that UTP stimulation activates PKC δ , a major nPKC isoform, on the lysosome surface.

Lysosomal DAG is critical for PKC activity at the lysosome

nPKCs are solely dependent on DAG for activation. We hypothesized that the lysosomal PKC δ activity demonstrated here is dependent on DAG on the lysosomal membrane. However, DAG has not been previously shown to accumulate on lysosome membranes. To test our hypothesis, we generated a lysosome-targeted DAG biosensor to directly probe DAG dynamics at this location. Starting with the existing PM-targeted DAG biosensor Digda⁴⁶, we replaced the C-terminal PM-targeting motif with the LAMP1 motif for lysosomal targeting and used the enhanced CFP Cerulean as the FRET donor (Supplementary Fig. 11a). The resulting Lyso-Digda sensor colocalized with LysoTracker

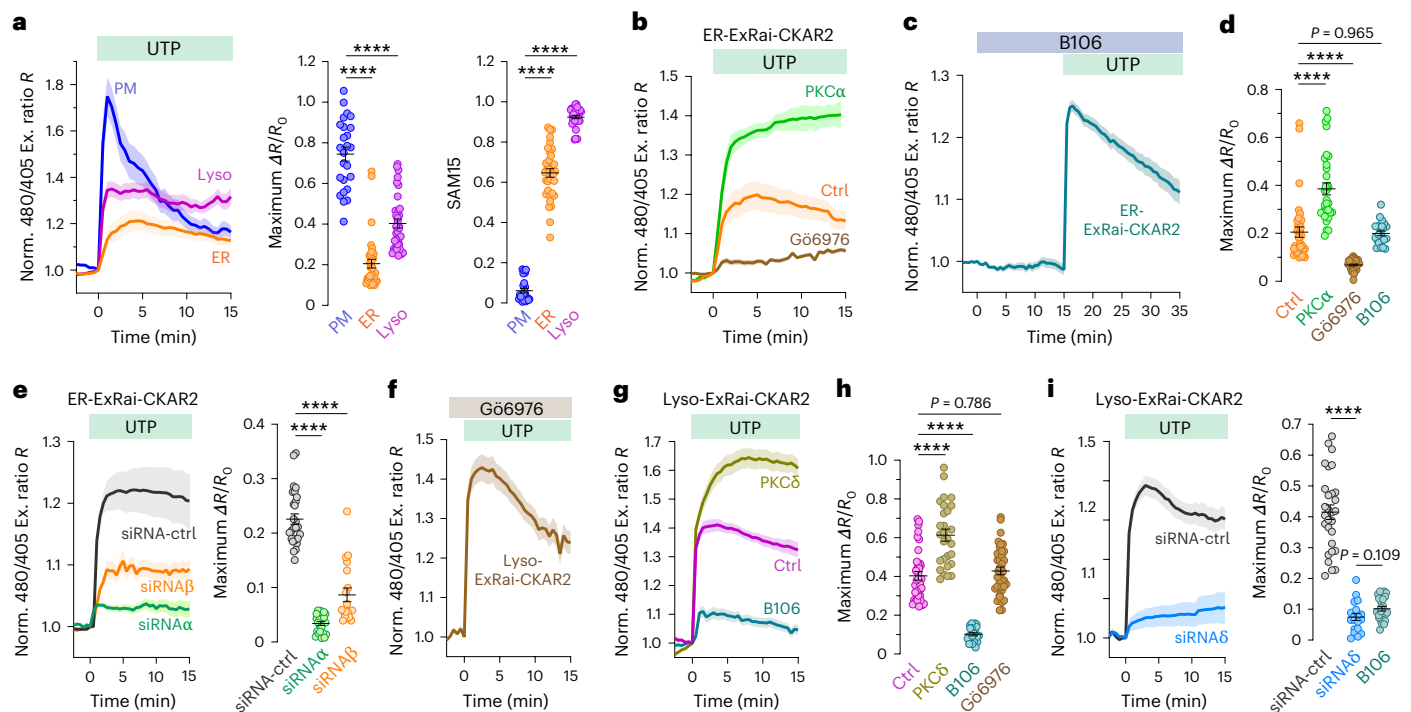


Fig. 3 | PKC regulation at the ER and lysosome. **a**, Representative average 480/405 excitation ratio time courses (hereafter, ‘time courses’) from UTP (100 μM)-stimulated Cos7 cells expressing PM-ExRai-CKAR2 ($n = 10$ cells), ER-ExRai-CKAR2 ($n = 15$ cells) or Lyso-ExRai-CKAR2 ($n = 16$ cells). Maximum responses ($\Delta R/R_0$) and SAM15 quantified from $n = 25$, $n = 36$ and $n = 36$ cells. **b,c**, ER-ExRai-CKAR2 response time courses from Cos7 cells without (Ctrl, $n = 10$ cells) or with (Gö6976, $n = 12$ cells) 30-min Gö6976 preincubation or coexpressing PKCα-mCherry (PKCα, $n = 14$ cells) stimulated with UTP (**b**) or with 5 μM B106 followed by UTP (**c**; $n = 15$ cells). **d**, Maximum responses quantified from $n = 36$ (Ctrl), $n = 34$ (Gö6976), $n = 23$ (B106) and $n = 32$ (PKCα) cells. **e**, ER-ExRai-CKAR2 response time courses from UTP-stimulated Cos7 cells cotransfected with control siRNA (scramble, $n = 18$ cells), PKCα siRNA ($n = 15$ cells) or PKCβ siRNA ($n = 9$ cells). Maximum responses quantified from $n = 28$ (siRNA-ctrl), $n = 24$ (siRNAα) and $n = 19$ (siRNAβ) cells. **f,g**, Lyso-ExRai-CKAR2 response time courses

from Cos7 cells pretreated with Gö6976 (1 μM) followed by UTP (**f**; $n = 16$ cells) or without (Ctrl, $n = 12$ cells) or with 30-min B106 pretreatment (B106, $n = 9$ cells) or coexpressing PKCδ-mCherry (**g**; PKCδ, $n = 12$ cells). **h**, Maximum responses quantified from $n = 36$ (Ctrl), $n = 37$ (Gö6976), $n = 21$ (B106) and $n = 28$ (PKCδ) cells. **i**, Lyso-ExRai-CKAR2 response time courses from UTP-stimulated Cos7 cells cotransfected with control siRNA (scramble, $n = 16$ cells) or PKCδ siRNA ($n = 12$ cells). Maximum responses quantified from $n = 29$ (siRNA-ctrl), $n = 19$ (siRNAδ) and $n = 24$ (B106) cells. Time courses are representative of three independent experiments; solid lines indicate mean responses and shaded areas indicate the s.e.m. Maximum responses and SAM15 levels were quantified from three independent experiments; data are the mean \pm s.e.m. **** $P < 0.0001$. Data were analyzed using ordinary one-way ANOVA followed by Dunnett’s multiple-comparison test.

Red-positive puncta in Cos7 cells, with a Pearson’s coefficient of 0.77 ± 0.05 (Supplementary Fig. 11b), and showed a $21\% \pm 1\%$ yellow/cyan (Y/C) emission ratio increase upon treatment with the phorbol ester phorbol 12,13-dibutyrate (PDBu) (Supplementary Fig. 11c; $n = 35$). Stimulating Lyso-Digda-expressing Cos7 cells with UTP led to a $9.4\% \pm 0.6\%$ emission ratio increase (Supplementary Fig. 11c; $n = 35$), suggesting that UTP induces DAG synthesis on the lysosomal membrane.

To determine whether lysosomal DAG is required for lysosomal PKC activity, we sought to selectively alter DAG levels on the lysosome membrane by targeted biochemical perturbation^{31,47}. DAG kinase ζ (DGKζ) catalyzes the conversion of DAG to phosphatidic acid and should be able to deplete basal DAG levels and suppress receptor-stimulated DAG accumulation at target sites (Fig. 4a). Indeed, when we targeted mRuby2-fused DGKζ to the lysosome using LAMP1 (Lyso-DGK), we recorded a significantly reduced Lyso-Digda basal emission ratio of 0.48 ± 0.09 in Lyso-DGK-coexpressing cells versus 0.6 ± 0.1 in control cells (Fig. 4a), suggesting that DAG basally accumulates on the lysosomal membrane. Lyso-DGK also blocked the UTP-induced Lyso-Digda response, yielding a $0.7\% \pm 0.3\%$ change in Y/C emission ratio (Supplementary Fig. 11d,e; $n = 32$). On the other hand, treatment with the nondegradable PDBu increased the Lyso-Digda emission ratio to 0.7 ± 0.1 in both the presence and the absence of Lyso-DGK (Fig. 4a), suggesting that Lyso-Digda can measure both basal and stimulated

DAG levels at the lysosome and that Lyso-DGK is effective in depleting lysosomal DAG.

The basal accumulation of DAG prompted us to investigate whether lysosomal nPKC is also basally active. Indeed, B106 addition induced a $28\% \pm 2\%$ decrease in excitation ratio on its own (Fig. 4b,d; $n = 38$), while neither Lyso-ExRai-CKAR2 T/A nor the cPKC inhibitor Gö6976 showed an observable effect, with changes in excitation ratio of $1.7\% \pm 0.7\%$ and $-0.2\% \pm 0.5\%$, respectively (Fig. 4b–d; $n = 35$ and 34), suggesting the presence of basal PKC activity on the lysosome. Overexpressing PKCδ also increased this basal lysosomal PKC activity, with B106 inducing a $49\% \pm 2\%$ decrease in Lyso-ExRai-CKAR2 signal (Fig. 4b,d; $n = 22$). Consistent with the observed effect on lysosomal DAG, we found that Lyso-DGK coexpression suppressed both the UTP-stimulated increase and the B106-induced decrease in the Lyso-ExRai-CKAR2 excitation ratio to $10\% \pm 1\%$ (Fig. 4e; $n = 22$) and $1.3\% \pm 0.8\%$ (Fig. 4f; $n = 44$), respectively. These data support our model that lysosomal PKC activity is dependent on lysosomal DAG, which is both basally present and dynamically produced in response to UTP (Supplementary Fig. 12).

Interestingly, thapsigargin (TG) alone induced a robust $37\% \pm 2\%$ increase in the Lyso-ExRai-CKAR2 excitation ratio (Fig. 4g; $n = 30$), suggesting that elevated Ca^{2+} is sufficient for lysosomal PKC activity. This effect was not associated with increased lysosomal DAG levels,

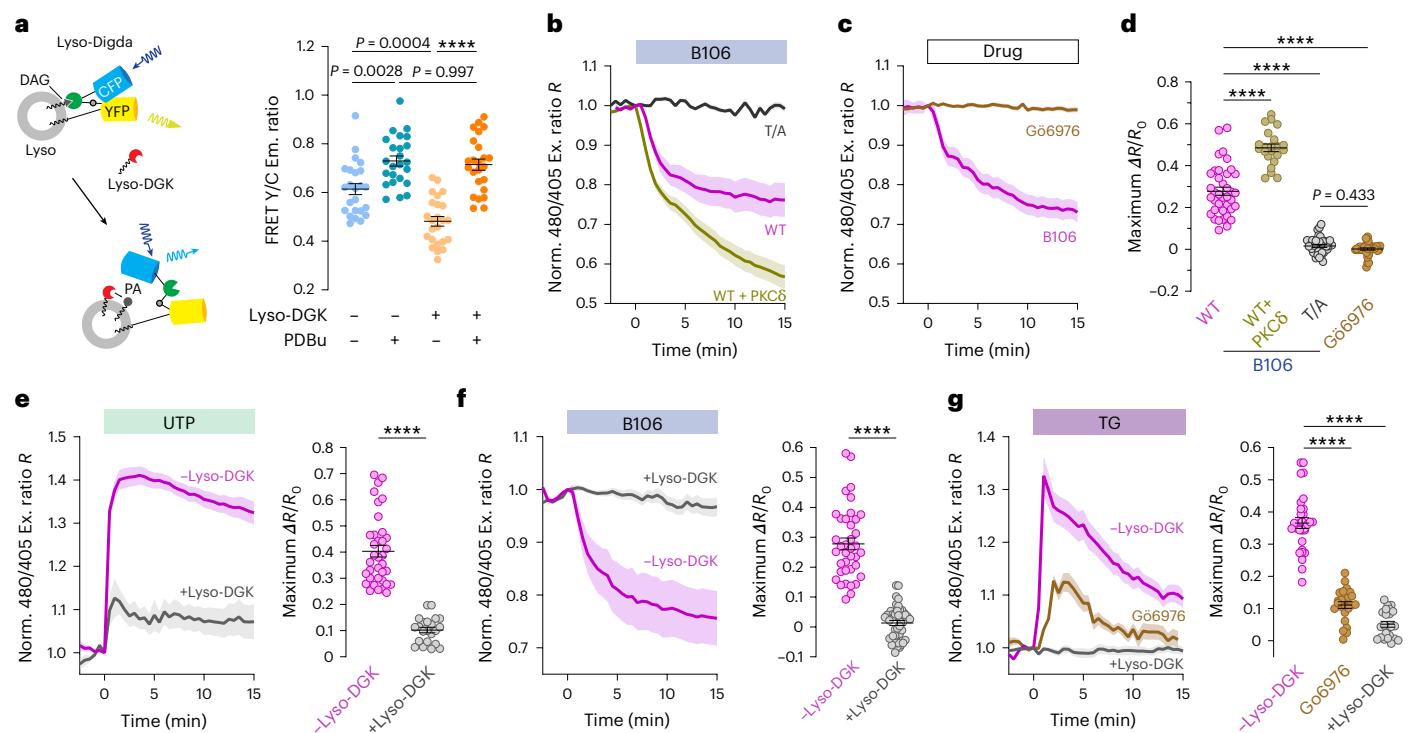


Fig. 4 | Lyosomal DAG is critical for lysosomal PKC activity. **a**, Detection and depletion of lysosomal DAG by Lyso-Digda and Lyso-DGK, respectively. Raw Y/C emission ratios from Lyso-Digda-expressing Cos7 cells with or without PDBu stimulation or Lyso-DGK coexpression ($n = 24$ cells each from three independent experiments; $P = 0.0028$, -Lyso-DGK/-PDBu versus -Lyso-DGK/+PDBu; $P = 0.0004$, -Lyso-DGK/-PDBu versus +Lyso-DGK/-PDBu). **b**, Representative average 480/405 excitation ratios time courses (hereafter, 'time courses') in Cos7 cells expressing Lyso-ExRai-CKAR2 (WT, $n = 18$ cells), Lyso-ExRai-CKAR2 T/A (T/A, $n = 16$ cells) or Lyso-ExRai-CKAR2 and PKC δ (+PKC δ , $n = 12$ cells) treated with $5 \mu\text{M}$ B106. **c**, Lyso-ExRai-CKAR2 response time courses in Cos7 cells treated with B106 (B106, $n = 18$ cells) or $1 \mu\text{M}$ G δ 6976 (G δ 6976, $n = 14$ cells). **d**, Maximum responses quantified from $n = 38$ (WT), $n = 22$ (WT + PKC δ), $n = 35$ (T/A) and $n = 34$ (G δ 6976) cells. **e**, Lyso-ExRai-CKAR2 response time courses from UTP ($100 \mu\text{M}$) stimulated Cos7 cells without (-Lyso-DGK, $n = 17$ cells) or with (+Lyso-DGK, $n = 10$

cells) Lyso-DGK coexpression. Maximum responses quantified from $n = 36$ and $n = 22$ cells. **f**, Lyso-ExRai-CKAR2 response time courses from Cos7 cells without (-Lyso-DGK, $n = 18$ cells) or with Lyso-DGK (+Lyso-DGK, $n = 20$ cells) coexpression and treated with B106. Maximum responses quantified from $n = 38$ and $n = 44$ cells. **g**, Lyso-ExRai-CKAR2 response time courses in TG-stimulated Cos7 cells without (-Lyso-DGK, $n = 10$ cells) or with Lyso-DGK (+Lyso-DGK, $n = 9$ cells) coexpression or with 30-min G δ 6976 (G δ 6976, $n = 11$ cells) pretreatment (TG). Maximum responses quantified from $n = 30$ (-Lyso-DGK), $n = 23$ (+Lyso-DGK) and $n = 24$ (G δ 6976) cells. Time courses are representative of three independent experiments; solid lines indicate mean responses and shaded areas indicate the s.e.m. Quantifications are from three independent experiments; data show the mean \pm s.e.m. **** $P < 0.0001$. Data were analyzed using ordinary one-way ANOVA followed by Tukey's multiple-comparisons test (**a**) or Dunnett's multiple-comparison test (**c,d,g**) or using a two-sided Student's *t*-test (**e,f**).

as Lyso-Digda showed only a $0.6\% \pm 0.5\%$ change in Y/C emission ratio upon TG stimulation (Supplementary Fig. 11d,e; $n = 21$). However, basal DAG enrichment on the lysosomal membrane appeared to be critical for this Ca^{2+} -induced lysosomal PKC activity, as overexpressing Lyso-DGK completely suppressed the TG-stimulated Lyso-ExRai-CKAR2 response to $0.1\% \pm 0.9\%$ (Fig. 4g; $n = 23$). Given that nPKCs are not directly responsive to Ca^{2+} , our data suggest that cPKC may also have a critical role in mediating lysosomal PKC activity. Indeed, pretreating cells with the cPKC-selective inhibitor G δ 6976 significantly reduced the TG-induced Lyso-ExRai-CKAR2 response to $11\% \pm 1\%$ versus no pretreatment (Fig. 4g; $n = 24$). Taken together, our data show that PKC exhibits complex subcellular regulation that is dependent on subcellular localization and stoichiometry of isoforms, as well as basal levels and spatiotemporal dynamics of second messengers.

aPKC regulation in polarized or lumenized 3D organoid models

aPKCs are unique among PKC isoforms in that they are activated by neither DAG nor Ca^{2+} but rather through binding to scaffold proteins. Binding of aPKC with a scaffold protein relieves autoinhibition by removing the pseudosubstrate from the substrate-binding cavity^{10,45}. For example, a major aPKC isoform, PKC ζ , adopts and maintains an open, active conformation through interactions with the cell

polarity-associated protein Par6. The PKC ζ -containing Par complex is an essential regulator of apical-basal polarity in epithelial cells²². aPKC regulates apical domain formation by phosphorylating and controlling various targets in specific cell domains, such as apical versus basal domains^{23,24}. Loss of apical-basal polarity has been shown to downregulate PKC ζ -mediated phosphorylation of SNAIL1 to promote EMT²². Direct interrogation of aPKC activity during epithelial polarization should, thus, provide critical insights into molecular and cellular processes involved in cancer metastasis. However, the modest activity of aPKC complicates efforts to directly measure endogenous aPKC activity in living cells.

Therefore, we tested the capability of ExRai-CKAR2 to detect aPKC activity by co-overexpressing an N-terminally truncated, constitutively active aPKC isoform, PKM ζ , with ExRai-CKAR2 or ExRai-CKAR2 T/A in HeLa cells. To visualize basal aPKC activity, we directly treated these cells with the aPKC-selective inhibitor pz09 (ref. 49) and quantified the subsequent decrease in biosensor signal. Upon pz09 treatment, ExRai-CKAR2 showed a $28.2\% \pm 0.9\%$ decrease in excitation ratio (Fig. 5a,c; $n = 24$), whereas ExRai-CKAR2 T/A showed a change of only $0.1\% \pm 0.1\%$ (Fig. 5b,c; $n = 28$). Strikingly, in the absence of PKM ζ overexpression, ExRai-CKAR2 showed a $12.4\% \pm 0.9\%$ decrease in excitation ratio in HeLa cells treated with $5 \mu\text{M}$ pz09, demonstrating robust detection of endogenous aPKC activity (Fig. 5b,c; $n = 24$),

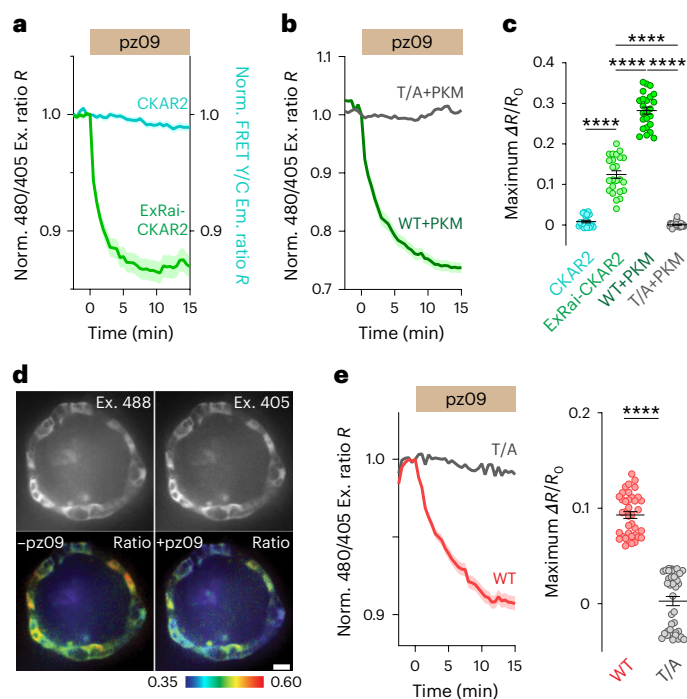


Fig. 5 | ExRai-CKAR2 reports endogenous aPKC activity in organoids.

a, Representative average 480/405 excitation ratio time courses (hereafter, ‘time courses’) or Y/C emission ratio responses in HeLa cells expressing ExRai-CKAR2 ($n = 24$ cells) or CKAR2 ($n = 20$ cells), respectively, treated with $5 \mu\text{M}$ pz09. **b**, Response time courses from HeLa cells coexpressing ExRai-CKAR2 (WT + PKM, $n = 24$ cells) or ExRai-CKAR2 T/A (T/A + PKM, $n = 28$ cells), along with mCherry-tagged constitutively active PKM ζ , and treated with $5 \mu\text{M}$ pz09. **c**, Maximum responses quantified from $n = 20$, $n = 24$, $n = 24$ and $n = 28$ cells. **d**, Representative fluorescence and pseudocolor images of 3D-cultured MDCK organoids stably expressing Cyto-ExRai-CKAR2. The pseudocolor images depict raw Cyto-ExRai-CKAR2 excitation ratios (Ex480/405); warmer colors indicate higher ratios. Scale bar, $20 \mu\text{m}$. **e**, Response time courses from 3D-cultured MDCK organoids expressing Cyto-ExRai-CKAR2 (WT, $n = 38$ cells) or Cyto-ExRai-CKAR2 T/A (T/A, $n = 40$ cells) and treated with pz09. Right, maximum responses quantified from $n = 38$ and $n = 40$ cells in four organoids. Time courses are representative of three independent experiments; solid lines indicate mean responses and shaded areas indicate the s.e.m. Quantifications are from three independent experiments; data show the mean \pm s.e.m. Data were analyzed using ordinary one-way ANOVA followed by Tukey’s multiple-comparisons test (**c**) or a two-sided Student’s *t*-test (**e**). **** $P < 0.0001$.

whereas CKAR2, the best-performing FRET-based PKC sensor, failed to capture endogenous basal aPKC activity, with a minimal $0.8\% \pm 0.4\%$ change in Y/C emission ratio that was not significantly different from baseline (Fig. 5a,c; $n = 20$).

The ability of ExRai-CKAR2 to detect endogenous aPKC activity opens the door to studying aPKC regulation under more physiological conditions, such as during epithelial polarity formation. To explore this possibility, we first tested Cyto-ExRai-CKAR2 during MDCK cell polarization. Widely used to study epithelial polarity, MDCK cells can form polarized epithelial organoids with intact apical–basal polarity in 3D Matrigel culture. To validate our approach, we first treated 2D-cultured MDCK cells expressing Cyto-ExRai-CKAR2 with $5 \mu\text{M}$ pz09 and observed a $16\% \pm 1\%$ decrease in excitation ratio (Supplementary Fig. 13; $n = 24$), whereas cells expressing ExRai-CKAR2 T/A showed no detectable response, with a change in excitation ratio of only $0.7\% \pm 0.3\%$ (Supplementary Fig. 13; $n = 23$). On the basis of these results, we next generated MDCK cells stably expressing Cyto-ExRai-CKAR2, which we cultured in 3D. After 9 days of growth on Matrigel, MDCK cells developed into polarized organoids with

the signature hollow lumen structure (Fig. 5d). Confocal microscopy of these polarized MDCK organoids revealed a robust $9.3\% \pm 0.4\%$ decrease in the Cyto-ExRai-CKAR2 excitation ratio upon pz09 addition ($n = 38$). Conversely, MDCK organoids generated from cells stably expressing Cyto-ExRai-CKAR2 T/A showed no response to pz09, with a minimal change in excitation ratio of $-0.3\% \pm 0.5\%$ (Fig. 5e and Supplementary Fig. 14; $n = 40$). Thus, ExRai-CKAR2 enables direct, real-time visualization of polarity-related endogenous aPKC activity with single-cell resolution in a 3D culture model.

Although Cyto-ExRai-CKAR2 successfully reported aPKC activity upon pz09 treatment, we sought to further enhance selectivity for aPKC activity by targeting ExRai-CKAR2 directly to the Par complex. Previous efforts using the PBI domain of Par6 to target isoform-specific aPKAR were unsuccessful in localizing the biosensor to the Par complex, as the signature punctate structures representing the Par complex were not observed^{10,50,51}. We, therefore, tested directly tethering ExRai-CKAR2 to full-length Par6 (Fig. 6a). Initial tests incorporating short linkers of only two or eight residues between Par6 and ExRai-CKAR2 resulted in poor pz09-induced responses (Supplementary Fig. 15). We ultimately found that inserting a flexible, 49-aa linker between Par6 and ExRai-CKAR2 yielded a sensor with a robust response to pz09 addition. The resulting Par6-ExRai-CKAR2 sensor localized to punctate structures⁵¹ when expressed in HeLa cells and colocalized with other Par complex components (namely, PKC ζ and Par3), showing Pearson’s coefficients of 0.93 ± 0.05 and 0.82 ± 0.07 , respectively (Supplementary Fig. 16).

Par6-ExRai-CKAR2 showed a larger $-19\% \pm 1\%$ change in excitation ratio (Fig. 6b,d; $n = 32$) than untargeted ExRai-CKAR2 upon pz09 treatment, demonstrating enhanced sensitivity for detecting endogenous aPKC activity, whereas Par6-ExRai-CKAR2 T/A showed no response to pz09 treatment, with $\Delta R/R_0 = -0.5\% \pm 0.5\%$ (Fig. 6b,d; $n = 25$). Upon overexpression of constitutively active PKM ζ , pz09 induced an even stronger $46\% \pm 2\%$ decrease in excitation ratio (Fig. 6c,d; $n = 28$), whereas co-overexpressing Par3 did not affect the sensor response, yielding a $-17\% \pm 1\%$ change in excitation ratio (Fig. 6c,d; $n = 23$). To rule out potential activation of aPKC by the targeting motif, Par6, we compared this result to a variant containing a Par6 A30D substitution that was shown to disrupt aPKC binding and activation¹⁰. Par6-A30D-ExRai-CKAR2 showed a comparable response to pz09 of $-16\% \pm 2\%$ (Supplementary Fig. 17; $n = 18$), suggesting Par6-ExRai-CKAR2 does not artificially activate aPKC.

Strikingly, Par6-ExRai-CKAR2 also showed a significantly smaller $47\% \pm 5\%$ change in excitation ratio in response to PMA stimulation, which should induce full cPKC and nPKC activation, compared to untagged ExRai-CKAR2 (Fig. 6e; $n = 20$). To quantify the selectivity of Par6-ExRai-CKAR2 toward aPKC over other PKC isoforms, we calculated the ratio of the pz09-induced (that is, aPKC) response versus the PMA-induced (that is, pan-PKC) response. Compared to Cyto-ExRai-CKAR2, which showed $\Delta R_{\text{pz09}}/\Delta R_{\text{PMA}} = 0.043$, Par6-ExRai-CKAR2 showed a marked tenfold greater selectivity toward aPKC, with $\Delta R_{\text{pz09}}/\Delta R_{\text{PMA}} = 0.44$, indicating a reduced potential for interference from other PKC isoforms in studies of native aPKC regulation.

Par6-ExRai-CKAR2 serves as an ideal tool to visualize aPKC regulation at the Par complex. Melanoma cell adhesion molecule, a membrane receptor endogenously expressed in HEK293 cells, has been shown to mediate apical–basal polarity-driven lumenogenesis in HEK293 organoids⁵². Although Cdc42, an upstream regulator of Par6–aPKC in polarity formation⁵³, was shown to be polarized in this lumenogenesis model, aPKC activity has not been characterized. The two aPKC isoforms in human cells, PKC ζ and PKC ι , have compensatory roles during polarity formation²². Consistently, siRNA knockdown of either PKC ι or PKC ζ in HEK293T cells yielded similar changes in excitation ratio of $-10.5\% \pm 0.9\%$ ($n = 18$) or $-8.0\% \pm 0.6\%$ ($n = 24$) upon pz09 treatment, whereas knocking down both isoforms reduced the Par6-ExRai-CKAR2 response to $-0.9\% \pm 0.5\%$ ($n = 19$), indicating that basal aPKC activity was completely abolished (Fig. 6f and Supplementary Fig. 18).

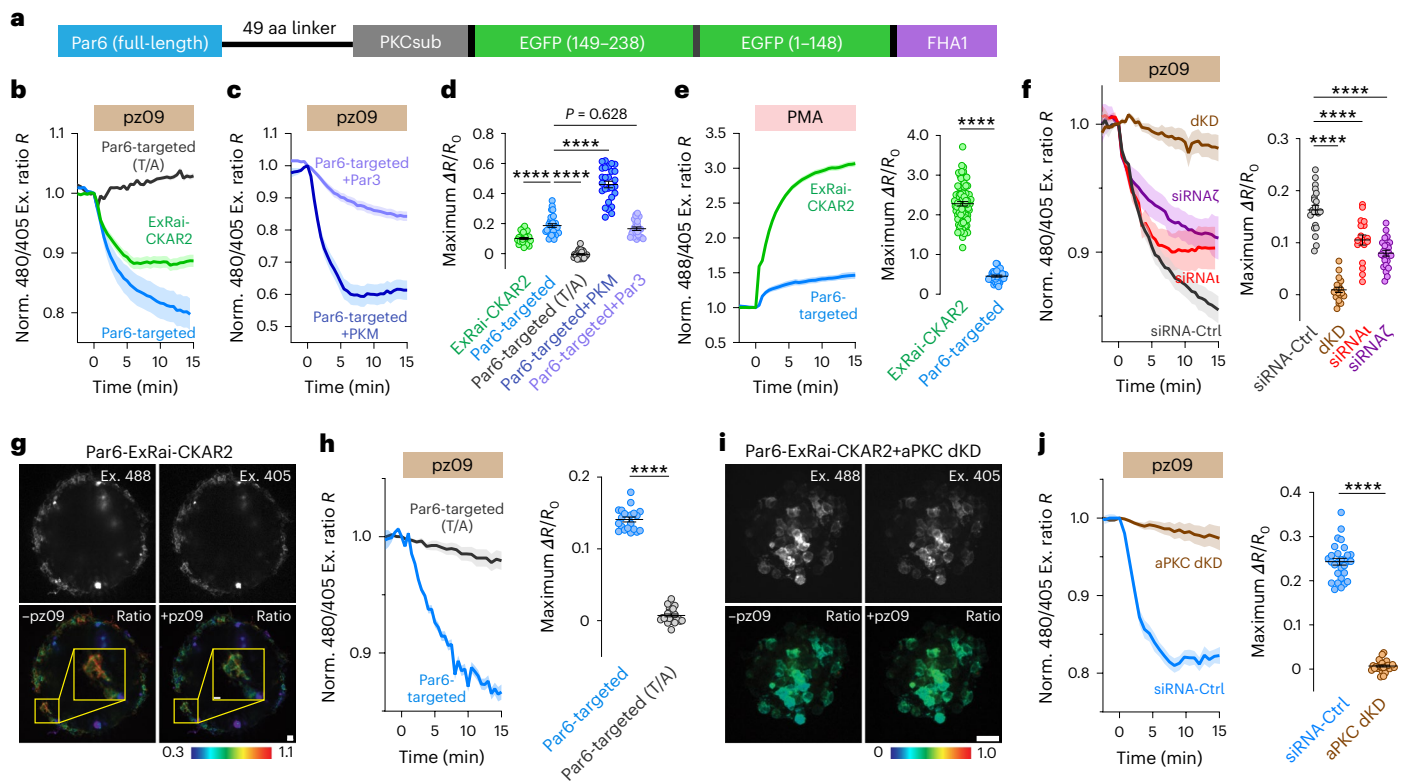


Fig. 6 | Targeted biosensor reports aPKC activity in lumenogenesis.

a, Par6-ExRai-CKAR2 domain structure. **b**, Representative average time courses of 480/405 excitation ratio (hereafter, 'time courses') in pzo9-treated HEK293T cells expressing ExRai-CKAR2 ($n = 28$ cells), Par6-ExRai-CKAR2 ($n = 20$ cells) or Par6-ExRai-CKAR2 T/A ($n = 18$ cells). **c**, Par6-ExRai-CKAR2 response time courses from pzo9-treated HEK293T cells coexpressing PKM ζ -mCherry (+PKM, $n = 28$ cells) or Par3-mCherry (+Par3, $n = 30$ cells). **d**, Maximum responses quantified from $n = 35$ (ExRai-CKAR2), $n = 32$ (Par6-ExRai-CKAR2), $n = 28$ (PKM ζ), $n = 23$ (Par3) and $n = 25$ (Par6-ExRai-CKAR2 T/A) cells. **e**, Response time courses from PMA-stimulated HEK293T cells expressing ExRai-CKAR2 ($n = 30$ cells) or Par6-ExRai-CKAR2 ($n = 20$ cells). Maximum responses quantified from $n = 80$ and $n = 32$ cells. **f**, Par6-ExRai-CKAR2 response time courses from pzo9-treated HEK293T cells cotransfected with control siRNA (control) or siRNA against PKC ζ , PKC ι or both (dKD). Maximum responses quantified from $n = 21$ (siRNA control), $n = 19$ (dKD), $n = 18$ (siRNA ι) and $n = 24$ (siRNA ζ) cells. **g**, Representative images showing Par6-ExRai-CKAR2-expressing HEK293T organoids under 405-nm or

488-nm excitation and excitation ratio response to pzo9 (pseudocolor). Scale bars, 20 μ m and 10 μ m (inset). **h**, Response time courses from pzo9-treated 3D-cultured HEK293T organoids expressing Par6-ExRai-CKAR2 ($n = 20$ cells) or Par6-ExRai-CKAR2 T/A ($n = 15$ cells). Maximum responses quantified from $n = 20$ and $n = 25$ cells in three organoids each. **i**, Par6-ExRai-CKAR2 with aPKC knockdown using siRNAs showing under 405-nm or 488-nm excitation and excitation ratio response to pzo9 (pseudocolor). Scale bar, 20 μ m. **j**, Par6-ExRai-CKAR2 response time courses from pzo9-treated HEK293T organoids coexpressing control siRNA or aPKC siRNA. Maximum responses quantified from $n = 29$ (WT) or $n = 28$ (dKD) cells from three organoids. Time courses are representative of three independent experiments; solid lines indicate mean responses and shaded areas indicate the s.e.m. Quantifications are from three independent experiments; data show the mean \pm s.e.m. **** $P < 0.0001$. Data were analyzed using ordinary one-way ANOVA followed by Tukey's multiple-comparisons test (**d, f**) or a two-sided Student's *t*-test (**e, h, j**).

Using Par6-ExRai-CKAR2, we were then able to confirm that aPKC is active during HEK293T lumenogenesis (Fig. 6g,h). In 3D-cultured HEK293T cells transiently expressing Par6-ExRai-CKAR2, pzo9 addition induced a $14.1\% \pm 0.3\%$ decrease in excitation ratio (Fig. 6g,h; $n = 20$), whereas ExRai-CKAR2 T/A showed no response (Fig. 6h and Supplementary Fig. 19). Dual knockdown of PKC ζ and PKC ι not only abolished basal aPKC activity, with the sensor showing a response of only $-0.7\% \pm 0.2\%$ ($n = 28$) versus $-24.3\% \pm 0.8\%$ ($n = 29$) for the control, but also disrupted lumen formation (Fig. 6i,j), suggesting that aPKC activity is indispensable for lumenogenesis. Together, these data demonstrate the potential for ExRai-CKAR2, particularly the Par-targeted variant, to promote our understanding of aPKC regulation during polarity and lumen formation.

Discussion

Genetically encoded fluorescent KARs are increasingly relied on to study the spatiotemporal regulation of signaling pathways in various settings, necessitating more extensive expansion of their versatility and advancement of their performance. Here, we introduced

ExRai-CKAR2, the most sensitive PKC activity reporter thus far, with a roughly 57-fold higher dynamic range compared to CKAR1 (ref. 28), 6-fold higher dynamic range compared to CKAR2 (ref. 35) and 4-fold higher dynamic range compared to ExRai-CKAR1 (ref. 34). In terms of signal-to-noise ratio (SNR), calculated by dividing the response amplitude by the s.d. of the baseline signal^{34,54–56}, ExRai-CKAR2 showed an SNR of $2.89/0.021 = 137.6$ versus $0.72/0.018 = 40$ for ExRai-CKAR1, similarly demonstrating a >3-fold performance improvement.

Subcellularly targeted ExRai-CKAR2s also exhibited roughly 20–150-fold higher PMA-induced responses compared to previous-generation targeted CKARs¹¹. The different PMA-stimulated maximum response amplitudes exhibited by subcellularly targeted ExRai-CKAR2s most likely stem from differences in basal PKC activity and local phosphatase activity at different locations. Indeed, differences in PM and cytosolic CKAR responses to phorbol ester were previously shown to originate from the different basal and phosphatase-suppressed PKC activities at these locations¹¹, with basal, stimulated and phosphatase-suppressed PKC activities adding up to similar levels. In addition, local steric hinderance may restrict conformational changes

in subcellularly targeted biosensors, resulting in smaller dynamic ranges. Similar effects were seen in other targeted biosensors, such as ExRai-AKAR targeted to the PM or other subcellular locations³⁰.

Nevertheless, the robust performance of ExRai-CKAR2 enables us to detect subtle PKC activity changes under physiological stimulation at different subcellular locations and to monitor endogenous aPKC activity in organoid models, which posed a challenge to previous PKC activity biosensors. By tuning the spacer length between the Par6-targeting domain and ExRai-CKAR2, we were able to obtain Par6-targeted biosensors that retain similar dynamic ranges as the untargeted sensor (Fig. 6d), empowering our efforts to dissect spatiotemporal PKC regulation. Future engineering will focus on generating isoform-specific biosensors and further increasing dynamic range. Overall, ExRai-CKAR2 represents notable progress in detecting subcellular PKC activity with high sensitivity and facilitates robust visualization of subtle PKC signaling dynamics with subcellular precision, even in 3D cultures.

PKC isoforms exhibit different, sometimes opposing, functions under various physiological and pathological conditions, including cancer development⁵⁷. This phenomenon has previously been attributed to cancer-specific or cell-type-specific differences^{1,5,45,58}. Using subcellularly targeted ExRai-CKAR2, we discovered that different PKC isoforms exhibit distinct spatial signatures. Although we detected PKC activity at the ER and lysosomes upon GPCR activation by UTP, we found that cPKCs were the primary contributor to ER-localized PKC activity, whereas nPKCs were the dominant isoform responsible for lysosomal PKC activity. Thus, PKC isoforms may drive specific functional effects by forming spatially distinct signaling territories.

The ability to sensitively detect subcellular PKC activities also enabled us to more closely investigate their regulation. The dominant role of cPKC in $G\alpha_q$ -protein-stimulated PKC activity at the ER is consistent with the activation of cPKC by Ca^{2+} and DAG, as well as previously observed localization of PKC α to the ER. Imaging and mass spectrometry analyses^{59,60} also indicated that DAG is enriched on ER membranes in oocytes and muscle cells. Meanwhile, a principal role for nPKC in lysosomal PKC activity is consistent with previous results showing the lysosomal localization of PKC δ (ref. 61). Although PLC, which catalyzes DAG production from phosphatidylinositol 4,5-bisphosphate, has been shown to localize to lysosomes and regulate lysosome stability^{62,63}, few studies have directly investigated lysosomal DAG accumulation. We discovered that DAG is not only present but also basally enriched on lysosome membranes, supporting both basal nPKC activity and Ca^{2+} -induced cPKC activation at this location, partially mirroring Golgi PKC signaling^{15,64}. However, how $G\alpha_q$ -protein-mediated signaling induces lysosomal DAG elevations remains unclear. In contrast to the Golgi, Ca^{2+} did not directly induce lysosomal DAG synthesis, suggesting that $G\alpha_q$ -protein-mediated lysosomal DAG production requires additional regulators. We recently showed that active GPCRs and $G\alpha_s$ at the endosome are critical for GPCR-mediated ERK activation⁶⁵. The $G\alpha_q$ -protein-coupled P2Y1 purinergic receptor has also been reported to traffic from the PM to the lysosome membrane through lysosomal sorting⁶⁶. Similar effects were also observed for other $G\alpha_q$ -coupled receptors, such as the δ opioid receptor⁶⁷. $G\alpha_q$ -coupled receptors are also recycled through the endosome-lysosome pathway⁶⁸. We speculate that the UTP receptor, also a P2Y-type purinergic receptor, could traffic to the lysosome after UTP stimulation and stimulate DAG synthesis by lysosomal PLC. However, it remains to be seen whether the UTP receptor remains active at this location to regulate lysosomal PLC.

Given their ability to mimic complex organs, cultured organoids are increasingly recognized as valuable in vitro models with huge clinical potential⁶⁹. The importance of Par-aPKC complexes in cell polarity formation and EMT has been well documented in these models, with more than half of all known polarity-regulating proteins identified as aPKC substrates^{22,24}. However, how aPKC is regulated by and

functionally integrates upstream signals in polarity formation is far less understood. Biosensors are ideal tools for visualizing the regulation and function of biochemical pathways in organoids⁷⁰ but their application has thus far been limited⁷¹. Responses from kinase translocation reporters, which traffic from the nucleus to the cytosol upon phosphorylation by specific kinases, are difficult to quantify in such a compact volumes⁷¹, whereas the modest dynamic ranges of FRET-based biosensors such as CKAR2 limit their sensitivity in 3D cultures. Thus, with its dramatically enhanced dynamic range, ExRai-CKAR2 represents a felicitous development in our efforts to provide a continuous and quantifiable readout of endogenous aPKC activity in 3D culture. Using ExRai-CKAR2, we were able to detect basal aPKC activity in polarized and lumenized organoids, consistent with previous findings^{22,52}. aPKCs are recruited to functionally distinct protein assemblies to drive cell polarity but their exact spatiotemporal regulation is unclear^{24,72}. By targeting ExRai-CKAR2 directly to Par6, we detected aPKC activity specifically at the Par complex and found that aPKC activity is enriched at this site, which is also shielded from cPKC and nPKC activities, an illustration of signaling compartmentation. These tools could, therefore, benefit research in aPKC regulation as it cycles between functional complexes in more complex systems, such as patient-derived organoid models, using advanced organoid imaging technologies, including lattice light-sheet microscopy.

Online content

Any methods, additional references, Nature Portfolio reporting summaries, source data, extended data, supplementary information, acknowledgements, peer review information; details of author contributions and competing interests; and statements of data and code availability are available at <https://doi.org/10.1038/s41589-024-01758-3>.

References

1. Dowling, C. M. et al. Protein kinase C β II suppresses colorectal cancer by regulating IGF-1 mediated cell survival. *Oncotarget* **7**, 20919–20933 (2016).
2. Antal, C. E. et al. Cancer-associated protein kinase C mutations reveal kinase's role as tumor suppressor. *Cell* **160**, 489–502 (2015).
3. Rask-Madsen, C. & King, G. L. Proatherosclerotic mechanisms involving protein kinase C in diabetes and insulin resistance. *Arterioscler. Thromb. Vasc. Biol.* **25**, 487–496 (2005).
4. Lorden, G. et al. Enhanced activity of Alzheimer disease-associated variant of protein kinase C α drives cognitive decline in a mouse model. *Nat. Commun.* **13**, 7200 (2022).
5. Van, A. N. et al. Protein kinase C fusion proteins are paradoxically loss of function in cancer. *J. Biol. Chem.* **296**, 100445 (2021).
6. Colgan, L. A. et al. PKC α integrates spatiotemporally distinct Ca^{2+} and autocrine BDNF signaling to facilitate synaptic plasticity. *Nat. Neurosci.* **21**, 1027–1037 (2018).
7. Lesley, A. C. et al. Dual regulation of spine-specific and synapse-to-nucleus signaling by PKC δ during plasticity. *J. Neurosci.* **43**, 5432 (2023).
8. Mochly-Rosen, D., Das, K. & Grimes, K. V. Protein kinase C, an elusive therapeutic target? *Nat. Rev. Drug Discov.* **11**, 937–957 (2012).
9. Newton, A. C. Protein kinase C: perfectly balanced. *Crit. Rev. Biochem. Mol. Biol.* **53**, 208–230 (2018).
10. Tobias, I. S. & Newton, A. C. Protein scaffolds control localized protein kinase C ζ activity. *J. Biol. Chem.* **291**, 13809–13822 (2016).
11. Gallegos, L. L., Kunkel, M. T. & Newton, A. C. Targeting protein kinase C activity reporter to discrete intracellular regions reveals spatiotemporal differences in agonist-dependent signaling. *J. Biol. Chem.* **281**, 30947–30956 (2006).
12. Enyedi, A. et al. Protein kinase C phosphorylates the 'a' forms of plasma membrane Ca^{2+} pump isoforms 2 and 3 and prevents binding of calmodulin. *J. Biol. Chem.* **272**, 27525–27528 (1997).

13. Verma, A. K., Paszty, K., Filoteo, A. G., Penniston, J. T. & Enyedi, A. Protein kinase C phosphorylates plasma membrane Ca²⁺ pump isoform 4a at its calmodulin binding domain. *J. Biol. Chem.* **274**, 527–531 (1999).
14. Blackshear, P. J. The MARCKS family of cellular protein kinase C substrates. *J. Biol. Chem.* **268**, 1501–1504 (1993).
15. Kajimoto, T., Sawamura, S., Tohyama, Y., Mori, Y. & Newton, A. C. Protein kinase C δ -specific activity reporter reveals agonist-evoked nuclear activity controlled by Src family of kinases. *J. Biol. Chem.* **285**, 41896–41910 (2010).
16. Sakaki, K. & Kaufman, R. J. Regulation of ER stress-induced macroautophagy by protein kinase C. *Autophagy* **4**, 841–843 (2008).
17. Chen, Y. J. et al. Involvement of protein kinase C in the inhibition of lipopolysaccharide-induced nitric oxide production by thapsigargin in RAW 264.7 macrophages. *Int. J. Biochem. Cell Biol.* **37**, 2574–2585 (2005).
18. Schmitz-Peiffer, C. Deconstructing the role of PKC epsilon in glucose homeostasis. *Trends Endocrinol. Metab.* **31**, 344–356 (2020).
19. Li, Y. et al. Protein kinase C controls lysosome biogenesis independently of mTORC1. *Nat. Cell Biol.* **18**, 1065–1077 (2016).
20. Larocca, M. C., Ochoa, E. J., Rodriguez Garay, E. A. & Marinelli, R. A. Protein kinase C-dependent inhibition of the lysosomal degradation of endocytosed proteins in rat hepatocytes. *Cell. Signal.* **14**, 641–647 (2002).
21. Horikoshi, Y. et al. Interaction between PAR-3 and the aPKC–PAR-6 complex is indispensable for apical domain development of epithelial cells. *J. Cell Sci.* **122**, 1595–1606 (2009).
22. Jung, H. Y. et al. Apical–basal polarity inhibits epithelial–mesenchymal transition and tumour metastasis by PAR-complex-mediated SNAIL1 degradation. *Nat. Cell Biol.* **21**, 359–371 (2019).
23. Martin-Belmonte, F. et al. Cell-polarity dynamics controls the mechanism of lumen formation in epithelial morphogenesis. *Curr. Biol.* **18**, 507–513 (2008).
24. Hong, Y. aPKC: the kinase that phosphorylates cell polarity. *F1000Res* **7**, 903 (2018).
25. Kajimoto, T. et al. Activation of atypical protein kinase C by sphingosine 1-phosphate revealed by an aPKC-specific activity reporter. *Sci. Signal.* **12**, eaat6662 (2019).
26. Gallegos, L. L. & Newton, A. C. Genetically encoded fluorescent reporters to visualize protein kinase C activation in live cells. *Methods Mol. Biol.* **756**, 295–310 (2011).
27. Antal, C. E. & Newton, A. C. Tuning the signalling output of protein kinase C. *Biochem. Soc. Trans.* **42**, 1477–1483 (2014).
28. Violin, J. D., Zhang, J., Tsien, R. Y. & Newton, A. C. A genetically encoded fluorescent reporter reveals oscillatory phosphorylation by protein kinase C. *J. Cell Biol.* **161**, 899–909 (2003).
29. Rutherford, C. et al. Regulation of cell survival by sphingosine-1-phosphate receptor S1P1 via reciprocal ERK-dependent suppression of Bim and PI-3-kinase/protein kinase C-mediated upregulation of Mcl-1. *Cell Death Dis.* **4**, e927 (2013).
30. Zhang, J. F. et al. An ultrasensitive biosensor for high-resolution kinase activity imaging in awake mice. *Nat. Chem. Biol.* **17**, 39–46 (2021).
31. Chen, M., Sun, T., Zhong, Y., Zhou, X. & Zhang, J. A highly sensitive fluorescent Akt biosensor reveals lysosome-selective regulation of lipid second messengers and kinase activity. *ACS Cent. Sci.* **7**, 2009–2020 (2021).
32. Schmitt, D. L. et al. Spatial regulation of AMPK signaling revealed by a sensitive kinase activity reporter. *Nat. Commun.* **13**, 3856 (2022).
33. Tsien, R. Y. The green fluorescent protein. *Annu. Rev. Biochem.* **67**, 509–544 (1998).
34. Mehta, S. et al. Single-fluorophore biosensors for sensitive and multiplexed detection of signalling activities. *Nat. Cell Biol.* **20**, 1215–1225 (2018).
35. Ross, B. L. et al. Single-color, ratiometric biosensors for detecting signaling activities in live cells. *eLife* **7**, e35458 (2018).
36. Ron, D. & Walter, P. Signal integration in the endoplasmic reticulum unfolded protein response. *Nat. Rev. Mol. Cell Biol.* **8**, 519–529 (2007).
37. Almanza, A. et al. Endoplasmic reticulum stress signalling—from basic mechanisms to clinical applications. *FEBS J.* **286**, 241–278 (2019).
38. Lawrence, R. E. & Zoncu, R. The lysosome as a cellular centre for signalling, metabolism and quality control. *Nat. Cell Biol.* **21**, 133–142 (2019).
39. Karunakaran, D., Tzahar, E., Liu, N., Wen, D. & Yarden, Y. Neu differentiation factor inhibits EGF binding. A model for trans-regulation within the ErbB family of receptor tyrosine kinases. *J. Biol. Chem.* **270**, 9982–9990 (1995).
40. Greenwald, E. et al. GPCR signaling measurement and drug profiling with an automated live-cell microscopy system. *ACS Sens.* **8**, 19–27 (2023).
41. Keyes, J. et al. Signaling diversity enabled by Rap1-regulated plasma membrane ERK with distinct temporal dynamics. *eLife* **9**, e57410 (2020).
42. Miranti, C. K., Ohno, S. & Brugge, J. S. Protein kinase c regulates integrin-induced activation of the extracellular regulated kinase pathway upstream of Shc. *J. Biol. Chem.* **274**, 10571–10581 (1999).
43. Saito, N. & Shirai, Y. Protein kinase C γ (PKC γ): function of neuron specific isotype. *J. Biochem.* **132**, 683–687 (2002).
44. Hayashi, K. & Altman, A. Protein kinase C θ (PKC θ): a key player in T cell life and death. *Pharmacol. Res.* **55**, 537–544 (2007).
45. Takashima, A. et al. Protein kinase C δ is a therapeutic target in malignant melanoma with NRAS mutation. *ACS Chem. Biol.* **9**, 1003–1014 (2014).
46. Nishioka, T. et al. Rapid turnover rate of phosphoinositides at the front of migrating MDCK cells. *Mol. Biol. Cell* **19**, 4213–4223 (2008).
47. Nelson, C. D. et al. Targeting of diacylglycerol degradation to M1 muscarinic receptors by β -arrestins. *Science* **315**, 663–666 (2007).
48. Graybill, C., Wee, B., Atwood, S. X. & Prehoda, K. E. Partitioning-defective protein 6 (Par-6) activates atypical protein kinase C (aPKC) by pseudosubstrate displacement. *J. Biol. Chem.* **287**, 21003–21011 (2012).
49. Trujillo, J. I. et al. 2-(6-Phenyl-1H-indazol-3-yl)-1H-benzo[d]imidazoles: design and synthesis of a potent and isoform selective PKC- ζ inhibitor. *Bioorg. Med. Chem. Lett.* **19**, 908–911 (2009).
50. Kono, K. et al. Reconstruction of Par-dependent polarity in apolar cells reveals a dynamic process of cortical polarization. *eLife* **8**, e45559 (2019).
51. Liu, Z. et al. Par complex cluster formation mediated by phase separation. *Nat. Commun.* **11**, 2266 (2020).
52. Gao, Q. et al. The signalling receptor MCAM coordinates apical–basal polarity and planar cell polarity during morphogenesis. *Nat. Commun.* **8**, 15279 (2017).
53. Martin-Belmonte, F. et al. PTEN-mediated apical segregation of phosphoinositides controls epithelial morphogenesis through Cdc42. *Cell* **128**, 383–397 (2007).
54. Nakamoto, C. et al. A novel red fluorescence dopamine biosensor selectively detects dopamine in the presence of norepinephrine in vitro. *Mol. Brain* **14**, 173 (2021).
55. Koveal, D. et al. A high-throughput multiparameter screen for accelerated development and optimization of soluble genetically encoded fluorescent biosensors. *Nat. Commun.* **13**, 2919 (2022).
56. Hires, S. A., Tian, L. & Looger, L. L. Reporting neural activity with genetically encoded calcium indicators. *Brain Cell Biol.* **36**, 69–86 (2008).

57. Newton, A. C. & Brognard, J. Reversing the paradigm: protein kinase C as a tumor suppressor. *Trends Pharmacol. Sci.* **38**, 438–447 (2017).
 58. Gökmen-Polar, Y., Murray, N. R., Velasco, M. A., Gatalica, Z. & Fields, A. P. Elevated protein kinase C β II is an early promotive event in colon carcinogenesis. *Cancer Res.* **61**, 1375–1381 (2001).
 59. Domart, M.-C. et al. Acute manipulation of diacylglycerol reveals roles in nuclear envelope assembly & endoplasmic reticulum morphology. *PLoS ONE* **7**, e51150 (2012).
 60. Perreault, L. et al. Intracellular localization of diacylglycerols and sphingolipids influences insulin sensitivity and mitochondrial function in human skeletal muscle. *JCI Insight* **3**, e96805 (2018).
 61. Ma, J. S., Haydar, T. F. & Radoja, S. Protein kinase C δ localizes to secretory lysosomes in CD8⁺ CTL and directly mediates TCR signals leading to granule exocytosis-mediated cytotoxicity. *J. Immunol.* **181**, 4716–4722 (2008).
 62. Wang, X., Zhao, H. F. & Zhang, G. J. Mechanism of cytosol phospholipase C and sphingomyelinase-induced lysosome destabilization. *Biochimie* **88**, 913–922 (2006).
 63. Matsuzawa, Y. & Hostetler, K. Y. Properties of phospholipase C isolated from rat liver lysosomes. *J. Biol. Chem.* **255**, 646–652 (1980).
 64. Carrasco, S. & Merida, I. Diacylglycerol-dependent binding recruits PKC θ and RasGRP1 C1 domains to specific subcellular localizations in living T lymphocytes. *Mol. Biol. Cell* **15**, 2932–2942 (2004).
 65. Kwon, Y. et al. Non-canonical β -adrenergic activation of ERK at endosomes. *Nature* **611**, 173–179 (2022).
 66. Does, M. R., Grimsey, N. J., Mendez, F. & Trejo, J. ALIX regulates the ubiquitin-independent lysosomal sorting of the P2Y1 purinergic receptor via a YPX3L motif. *PLoS ONE* **11**, e0157587 (2016).
 67. Tanowitz, M. & von Zastrow, M. Ubiquitination-independent trafficking of G protein-coupled receptors to lysosomes. *J. Biol. Chem.* **277**, 50219–50222 (2002).
 68. Plouffe, B., Thomsen, A. R. B. & Irannejad, R. Emerging role of compartmentalized G protein-coupled receptor signaling in the cardiovascular field. *ACS Pharm. Transl. Sci.* **3**, 221–236 (2020).
 69. Kim, J., Koo, B. K. & Knoblich, J. A. Human organoids: model systems for human biology and medicine. *Nat. Rev. Mol. Cell Biol.* **21**, 571–584 (2020).
 70. Keshara, R., Kim, Y. H. & Grapin-Botton, A. Organoid imaging: seeing development and function. *Annu. Rev. Cell Dev. Biol.* **38**, 447–466 (2022).
 71. Ponsioen, B. et al. Quantifying single-cell ERK dynamics in colorectal cancer organoids reveals EGFR as an amplifier of oncogenic MAPK pathway signalling. *Nat. Cell Biol.* **23**, 377–390 (2021).
 72. Rodriguez, J. et al. aPKC cycles between functionally distinct PAR protein assemblies to drive cell polarity. *Dev. Cell* **42**, 400–415 e9 (2017).
- Publisher's note** Springer Nature remains neutral with regard to jurisdictional claims in published maps and institutional affiliations.
- Springer Nature or its licensor (e.g. a society or other partner) holds exclusive rights to this article under a publishing agreement with the author(s) or other rightsholder(s); author self-archiving of the accepted manuscript version of this article is solely governed by the terms of such publishing agreement and applicable law.
- © The Author(s), under exclusive licence to Springer Nature America, Inc. 2024

Methods

Materials

PMA (LC Labs, P-1680), PDBu (LC Labs, P-4833), Gö6983 (MilliporeSigma, G1918), Gö6976 (MilliporeSigma, 365250), BAPTA-AM (Life Technologies, B6769), TG (Cayman Chemical, 10522), ionomycin (MilliporeSigma, 407951), B106 (Axon, 2981, 98%) and pz09 (Reagency, RNCY0048) were reconstituted in DMSO (Sigma-Aldrich) as 1,000× stock solutions. UTP (Alfa, >98%, J63427) was reconstituted in ultrapure water (MilliQ). Lipofectamine 2000 (11668019) was purchased from Thermo Fisher Scientific. LysoTracker Red (L7528) was purchased from Thermo Fisher Scientific and diluted in DMSO.

Plasmids

All primers used for molecular cloning are listed in Supplementary Table 2. To generate ExRai-CKAR linker variants, DNA fragments encoding cpEGFP, FHA1 and linkers were digested from pRRET-B ExRai-AKAR linker variants³⁰ with SacI and EcoRI (Thermo Fisher Scientific, FD1134 and FD0275, respectively) and then ligated into a SacI + EcoRI-digested pRRET-B ExRai-CKAR1 backbone. pRSET-B ExRai-CKAR linker variants were then subcloned into pcDNA3 using BamHI (Thermo Fisher Scientific, FD1464) and EcoRI digestion. ExRai-CKAR2 T/A was generated by Gibson assembly using NEBuilder HiFi DNA assembly kit (New England Biolabs E2621) and primers 1–2. ExRai-CKAR2 receptors targeting the PM, ER and lysosome were made by subcloning a BamHI + EcoRI-digested fragment encoding full-length ExRai-CKAR2 into BamHI + EcoRI-digested pcDNA3 backbones containing the N-terminal 11 amino acids from Lyn (MGCIKSKRKDK), the N-terminal 27 amino acids from CYP450 (MDPVVVLGLCLSLLLLLSLWKQSYGGG) or the targeted domain derived from full-length LAMP1 (ref. 31). Cyto-ExRai-CKAR2 was constructed by subcloning a BamHI + XhoI-digested fragment into BamHI + XhoI-digested pcDNA3 containing a C-terminal NES (LPPLERLTL). Par6-8aa-ExRai-CKAR2 was generated by Gibson assembly of a Par6 fragment, PCR-amplified from pKMyC-Par6C (a gift from I. Macara; Addgene, plasmid 15474)⁷³ using primers 3 and 4 to contain BspEI and BamHI restriction sites and a GGATGCTGGT spacer into HindIII + BamHI-digested pcDNA3.1(+)-ExRai-CKAR2. A truncated EV49 linker containing BspEI and BamHI flanking sequences was PCR-amplified from EKAR4 (ref. 41) using primers 5 and 6 and inserted into BspEI + BamHI-digested Par6-ExRai-CKAR2 to obtain Par6-ExRai-CKAR2 with a 49-aa flexible linker. Lyso-DGK-mRuby2 was made by Gibson assembly of DNA fragments encoding DGKζ (a gift from S. Gee; Addgene, plasmid 85454)⁷⁴ and mRuby2 (ref. 75) and PCR-amplified using primers 7–10 into a BamHI + XbaI-digested pcDNA3 backbone containing full-length LAMP1.

To make Lyso-Digda, the CFP of Digda was first replaced with ddrFP³⁴ to reduce FP homology and facilitate further cloning. The DNA encoding ddrFP was amplified by PCR using primers 11 and 12, digested with EcoRI and XhoI and ligated into the Digda plasmid⁴⁶ digested with the same enzymes. Then, the DNA fragment containing ddrFP-PKCβ2C1-Venus-KRasCT and all ERK rigid linkers was PCR-amplified using primers 13 and 14 to introduce a 3' EcoRI site. A modified pcDNA3 backbone was PCR-amplified using primers 15 and 16 to remove the existing EcoRI site add a new EcoRI restriction site after XbaI. These two fragments were combined using Gibson assembly to yield a modified ddrFP-PKCβ2C1-Venus-KrasCT plasmid. The LAMP1-targeting domain was PCR-amplified using primers 17 and 18, followed by XbaI and EcoRI digestion and insertion into XbaI + EcoRI-digested ddrFP-PKCβ2C1-Venus-KRasCT plasmid to replace the KRasCT. Cerulean (together with any 5' extension that exists in both parental and target plasmids) was PCR-amplified from Cer-FHA1-NES⁷⁶ using primers 19 and 20, digested with HindIII and XhoI and ligated into HindIII + XhoI-digested PKCβ2C1-Venus-LAMP1.

For the generation of MDCK stable cell lines, Cyto-ExRai-CKAR2 and Cyto-ExRai-CKAR2 T/A were PCR-amplified using forward primer

AAGCTTGGCGCCGCCACCA and reverse primer GGGCCCTCTAGATTA-CAG, digested with XbaI and then ligated into EcoRV + XbaI-digested pLV-puro lentivirus vector. All plasmids were confirmed by DNA sequencing (Genewiz).

Expression and purification of ExRai-CKAR2

His-tagged ExRai-CKAR2 in pRSET-B vector was transformed into *Escherichia coli* BL21(DE3) chemically competent cells and a single colony was inoculated in 20 ml of Luria–Bertani (LB) medium containing ampicillin (100 μg ml⁻¹) and then cultured overnight at 37 °C with shaking. The seed culture was inoculated to 1 L of LB–ampicillin medium. The culture was shaken vigorously (220 r.p.m.) at 37 °C until reaching an optical density at 600 nm of 0.6–0.8. ExRai-CKAR2 expression was induced by IPTG addition to a final concentration of 200 μM, followed by shaking at 18 °C for 20 h. Cells were harvested by centrifugation (5,000g, 10 min, 4 °C) and stored at –80 °C until harvesting.

Frozen cell pellets were thawed on ice before resuspension in lysis buffer (50 mM Tris pH 7.4, 300 mM NaCl, 10% glycerol and 10 mM DTT) containing 1 mM PMSF and cOmplete protease inhibitor cocktail (Roche). Bacteria were then lysed by probe sonication at 100% power and ten cycles of 30 s on and 1 min off on ice. Cell debris was removed by centrifugation (45,000g for 0.5 h, 4 °C) and the supernatant was loaded onto a prepacked column with 5 ml of Hispur nickel nitrilotriacetic acid resin (Ni-NTA, GE Healthcare) through a syringe at roughly 1 ml min⁻¹. The column was washed with lysis buffer containing 20 mM imidazole (20 ml) and then with 50 ml of washing buffer (50 mM Tris pH 7.4, 300 mM NaCl, 10% glycerol and 60 mM imidazole) using syringes at roughly 3 ml min⁻¹. The desired protein was eluted with lysis buffer supplemented with 250 mM imidazole. Fractions were analyzed by SDS–PAGE and the purest fractions were pooled, concentrated using Amicon Ultra-15 centrifugal columns (30-kDa cutoff, Millipore) and washed three times to exchange the buffer to 50 mM Tris pH 7.4, 300 mM NaCl and 10% glycerol. Protein concentrations were determined using the Pierce BCA protein assay kit (Thermo Fisher Scientific) on a Spark 20M microplate reader (Tecan).

In vitro excitation and emission spectra were obtained on a PTI QM-400 fluorometer using FelixGX version 4.1.2 software (Horiba). Excitation scans were collected at 530-nm emission and emission scans were performed at 405-nm and 480-nm excitation. Purified biosensor (1 μM) was incubated with 5 μg of PKCα for 30 min at 37 °C in kinase assay buffer (20 mM HEPES pH 7.4, 2 mM DTT, 5 mM MgCl₂) without ATP or lipids and with 500 μM EGTA (no Ca²⁺) for unphosphorylated spectra or with 100 μM ATP, phosphatidylserine (140 μM)–DAG (3.8 μM) membranes and 100 μM Ca²⁺ (no EGTA) for phosphorylated spectra. Data were analyzed with Excel.

Cell culture and transfection

All cells were cultured under standard conditions as previously described³⁰. HeLa (American Type Culture Collection (ATCC), CCL-2), HEK293T (ATCC, CRL-3216) and Cos7 (ATCC, CRL-1651) cells were cultured in DMEM (Gibco) containing 1 g L⁻¹ (HeLa) or 4.5 g L⁻¹ (HEK293T and Cos7) glucose, 10% (v/v) FBS (Sigma) and 1% (v/v) penicillin–streptomycin (Sigma-Aldrich). MDCK cells were cultured in MEM (Sigma) containing 10% (v/v) FBS (Sigma) and 1% (v/v) penicillin–streptomycin (Sigma-Aldrich).

All cells were maintained at 37 °C in a humidified atmosphere of 5% CO₂. For imaging experiments, cells were plated onto sterile 35-mm glass-bottomed dishes and grown to 50–70% confluence. Transient transfection was performed using Lipofectamine 2000 (Invitrogen, HeLa) or PolyJet (SigmaGen, HEK293T and Cos7) following the manufacturer's protocols, after which cells were cultured for an additional 24 h.

Biosensor localization

Cos7 cells expressing lysosome-targeted or ER-targeted ExRai-CKAR2 were stained for 30 min with LysoTracker RED (Invitrogen) at a final

concentration of 1 mM in Hank's balanced salt solution (HBSS) (Gibco) or coexpressed with ER-mRuby2, respectively. Cells were imaged on a Nikon Ti2 spinning-disk confocal microscope (Nikon Instruments) equipped with an SR HP APO TIRF $\times 100$ (1.49 numerical aperture (NA)) oil objective (Nikon), excitation disk CSU-X1 (Yokogawa) and a Photometrics Prime95B scientific complementary metal-oxide-semiconductor (sCMOS) camera (Photometrics) controlled by NIS-Elements software (high-content analysis package, Nikon). ExRai-CKAR2 images were acquired using 488-nm and 405-nm lasers at 15% and 20% power, respectively, and 200-ms exposure times. Red fluorescent protein (RFP) images were acquired using a 561-nm laser at 20% power and 200-ms exposure time.

MDCK stable cell line generation and organoid culture

MDCK stable cell lines were generated using lentiviral plasmid vectors. Briefly, 293T cells were transfected with pCMV $\Delta 8.2R$, VSVG and pLV-Puro lentiviral construct expressing Cyto-ExRai-CKAR2 or Cyto-ExRai-CKAR2 T/A. Viral supernatants were then concentrated using Lenti-X concentrators (Takara). Concentrated viral supernatants were applied to MDCK cells with $6 \mu\text{g ml}^{-1}$ protamine sulfate. Infection was repeated the next day. Infected cells were then selected with puromycin ($2 \mu\text{g ml}^{-1}$).

MDCK cells were grown in 3D culture as previously described⁷⁷. Briefly, Matrigel (growth factor reduced, BD Biosciences) was plated onto a 35-mm glass-bottom dish and allowed to solidify for 30 min at 37 °C. MDCK cells were trypsinized, resuspended in medium supplemented with 2% Matrigel and then plated on top of Matrigel.

Time-lapse fluorescence imaging

Cells were washed twice with HBSS supplemented with 20 mM HEPES pH 7.4 and glucose (2g L^{-1}) and subsequently imaged in the same buffer at room temperature. PMA, PDBu, UTP, Gö6983, Gö6976 or B106 was added as indicated. HeLa and Cos7 cells were imaged using established methods³¹ on a Zeiss AxioObserver Z7 microscope (Carl Zeiss) equipped with a Definite Focus.2 system (Carl Zeiss), a $\times 40$ (1.4 NA) oil objective and a Photometrics Prime95B sCMOS camera (Photometrics) controlled by METAFLUOR 7.7 software (Molecular Devices). Dual GFP excitation ratio imaging was performed using 480DF20 and 405DF20 excitation filters, a 505DRLP dichroic mirror and a 535DF50 emission filter. RFP intensity was imaged using a 572DF35 excitation filter, a 594DRLP dichroic mirror and a 645DF75 emission filter. Dual Y/C emission ratio imaging was performed using a 420DF20 excitation filter, a 455DRLP dichroic mirror and two emission filters (473DF24 for CFP and 535DF25 for YFP). Filter sets were alternated by an LEP MAC6000 control module (Ludl Electronic Products). Exposure times ranged from 100 to 500 ms and images were acquired every 30 s.

MDCK cells were imaged on the same system, controlled by a modified version of the open-source MATLAB (Mathworks) and μ manager (Micro-Manager)-based MATScope imaging suite³².

MDCK organoids were imaged on a Nikon Ti2 spinning-disk confocal microscope (Nikon Instruments) equipped with a CFI Apo LWD Lambda S $\times 40$ (1.15 NA) water immersion objective (Nikon), excitation disk CSU-X1 (Yokogawa) under SoRa mode and a Photometrics Prime95B sCMOS camera (Photometrics) controlled by NIS-Elements software (high-content analysis package, Nikon). ExRai-CKAR2 images were acquired using 488-nm and 405-nm lasers at 20% and 15% power, respectively, with 500-ms exposure times every 45 s.

Raw fluorescence images were analyzed as previously reported³⁴. Briefly, images were first corrected by subtracting the background fluorescence intensity of a cell-free region from the emission intensities of biosensor-expressing cells at each time point. Regions of interest based on sensor targeting were selected for analysis. The GFP excitation ratio (480/405, for ExRai biosensors), Y/C emission ratio (for FRET-based biosensors) or RFP intensity was then calculated at each time point. All biosensor response time courses were subsequently plotted as the

normalized fluorescence intensity or ratio change with respect to time zero ($\Delta F/F_0$ or $\Delta R/R_0$), calculated as $(F - F_0)/F_0$ or $(R - R_0)/R_0$, where F and R are the fluorescence intensity and ratio value at a given time point and F_0 and R_0 are the initial fluorescence intensity or ratio value at time zero, which was defined as the time point immediately preceding drug addition. Changes in maximum intensity ($\Delta F/F$) or ratio ($\Delta R/R$) were calculated as $(F_{\text{max}} - F_{\text{min}})/F_{\text{min}}$ or $(R_{\text{max}} - R_{\text{min}})/R_{\text{min}}$, where F_{max} and F_{min} or R_{max} and R_{min} are the maximum and minimum intensity or ratio value recorded after stimulation, respectively. Graphs were plotted using GraphPad Prism 8 (GraphPad Software).

PKC isoform knockdown

On-TARGETplus SMARTpool siRNAs against PKC α , PKC β , PKC δ and scramble control were purchased from Dharmacon; siRNAs against PKC ζ and PKC ι were purchased from Santa Cruz Biotechnology. For siRNA knockdown in 2D cell cultures, 500 pmol of each siRNA was cotransfected with biosensor(s) into cells plated onto sterile 35-mm glass-bottom dishes using Lipofectamine 2000 (Invitrogen, for Cos7) or PolyJet (Signagen, for HEK293T), after which cells were cultured for an additional 48 h before imaging and western blotting experiments. For siRNA knockdown in 3D HEK293T organoids, 500 pmol of each siRNA was cotransfected with biosensor(s) into cells 24 h before seeding in Matrigel using PolyJet and then transfected into organoids again 72 h before imaging experiments.

Immunoblotting

After siRNA knockdown and imaging experiments, the same dish of cells were immunoblotted similar to previous methods³¹. Briefly, cells were washed with ice-cold PBS and then lysed in radioimmunoprecipitation assay lysis buffer containing protease inhibitor cocktail (Roche), 1 mM PMSF, 1 mM Na_3VO_4 , 1 mM NaF and 25 nM calyculin A. Total cell lysates were incubated on ice for 30 min before centrifuged at $15,000g$ at 4 °C for 20 min. Protein concentration in each sample was determined by BCA assay (Pierce). Equal amounts of total protein were separated by 4–15% SDS-PAGE and transferred to PVDF membranes. The membranes were blocked with TBS containing 0.1% Tween-20 and 5% BSA and then incubated with primary antibodies overnight at 4 °C. The next day, membranes were washed, incubated with the appropriate horseradish peroxidase-conjugated secondary antibodies and developed using horseradish peroxidase-based chemiluminescent substrate (34579 and 34076, Thermo Fisher Scientific). The following primary antibodies were used for immunoblotting: anti-PKC α (610108), anti-PKC β (610128), anti-PKC δ (610397) and anti-PKC ι (610175) from BD Biosciences, anti-PKC ζ (17781) from Santa Cruz Biotechnology and anti-GAPDH (2118) from Cell Signaling Technology. All primary antibodies were used at 1:1,000 dilution. Horseradish peroxidase-labeled goat anti-rabbit (PI31460) or anti-mouse (PI31430) secondary antibodies were purchased from Pierce. All secondary antibodies were used at 1:2,000 dilution.

Statistics and reproducibility

All experiments were independently repeated as noted in the figure legends. Statistical analyses were performed using GraphPad Prism 8. For Gaussian data, Student's t -test was used for pairwise comparisons. For comparing three or more sets of data, ordinary one-way analysis of variance (ANOVA) followed by a multiple-comparisons test was performed. Statistical significance was defined as $P < 0.05$ with a 95% confidence interval. The number of cells analyzed and number of independent experiments are reported in all figure legends. All time courses and scattered plots shown depict the mean \pm s.e.m. unless otherwise noted.

Reporting summary

Further information on research design is available in the Nature Portfolio Reporting Summary linked to this article.

Data availability

The data that support the findings of this study are available within the main text and Supplementary Information. Data are also available from the corresponding author upon request. Source data are provided with this paper.

Code availability

Custom ImageJ macros and MATLAB code used to analyze imaging data are available on GitHub (<https://github.com/jinzhanglab-ucsd/MatScopeSuite>)³².

References

73. Joberty, G., Petersen, C., Gao, L. & Macara, I. G. The cell-polarity protein Par6 links Par3 and atypical protein kinase C to Cdc42. *Nat. Cell Biol.* **2**, 531–539 (2000).
74. Hogan, A. et al. Interaction of γ 1-syntrophin with diacylglycerol kinase- ζ . Regulation of nuclear localization by PDZ interactions. *J. Biol. Chem.* **276**, 26526–26533 (2001).
75. Zhang, J. Z. et al. Phase separation of a PKA regulatory subunit controls cAMP compartmentation and oncogenic signaling. *Cell* **182**, 1531–1544 (2020).
76. Herbst, K. J., Allen, M. D. & Zhang, J. Luminescent kinase activity biosensors based on a versatile bimolecular switch. *J. Am. Chem. Soc.* **133**, 5676–5679 (2011).
77. Debnath, J., Muthuswamy, S. K. & Brugge, J. S. Morphogenesis and oncogenesis of MCF-10A mammary epithelial acini grown in three-dimensional basement membrane cultures. *Methods* **30**, 256–268 (2003).

Acknowledgements

We thank all members of the Zhang lab, especially Y. Zhong, for technical help and discussion of the paper and J. Hardy for help with artwork. We thank E. Griffis and P. Guo of the UCSD Nikon Imaging Center for assistance with confocal imaging, T. Hoang for his technical help with cloning and G. Lorden Losada from the A.C.N. lab for providing purified PKC α and technical support with in vitro

characterization of ExRai-CKAR2. This work is supported by National Institutes of Health grants R35 CA197622, R01 CA262815 and RF1 MH126707 (to J.Z.), R35 GM122523 (to A.C.N.) and R01 CA236386, R01 CA174869 and R01 CA262794 (to J.Y.), as well as by a TRDRP Postdoctoral Fellowship (T32FT5342) to Q.S.

Author contributions

Q.S., S.M., J.Y. and Jin Zhang conceptualized the project. J.-F.Z. and S.M. performed the linker screening and generated ExRai-CKAR2. Q.S. performed the in vitro characterization of ExRai-CKAR2, generated the other constructs and performed all live-cell and organoid imaging. Jing Zhang and Q.S. generated ExRai-CKAR2 and Cyto-ExRai-CKAR2 stable MDCK cell lines. Jing Zhang generated MDCK organoids. Q.S. generated HEK293T organoids. A.C.N., J.Y. and Jin Zhang supervised the project and coordinated experiments. Q.S. and Jing Zhang analyzed the data. Q.S., Jing Zhang, W.L., S.M. and Jin Zhang wrote the paper. All authors read and agreed on the final paper.

Competing interests

The authors declare no competing interests.

Additional information

Supplementary information The online version contains supplementary material available at <https://doi.org/10.1038/s41589-024-01758-3>.

Correspondence and requests for materials should be addressed to Jin Zhang.

Peer review information *Nature Chemical Biology* thanks Jerome Fox, Chonglin Yang and the other, anonymous reviewer(s) for their contribution to the peer review of this work.

Reprints and permissions information is available at www.nature.com/reprints.

Reporting Summary

Nature Portfolio wishes to improve the reproducibility of the work that we publish. This form provides structure for consistency and transparency in reporting. For further information on Nature Portfolio policies, see our [Editorial Policies](#) and the [Editorial Policy Checklist](#).

Statistics

For all statistical analyses, confirm that the following items are present in the figure legend, table legend, main text, or Methods section.

n/a | Confirmed

- The exact sample size (n) for each experimental group/condition, given as a discrete number and unit of measurement
- A statement on whether measurements were taken from distinct samples or whether the same sample was measured repeatedly
- The statistical test(s) used AND whether they are one- or two-sided
Only common tests should be described solely by name; describe more complex techniques in the Methods section.
- A description of all covariates tested
- A description of any assumptions or corrections, such as tests of normality and adjustment for multiple comparisons
- A full description of the statistical parameters including central tendency (e.g. means) or other basic estimates (e.g. regression coefficient) AND variation (e.g. standard deviation) or associated estimates of uncertainty (e.g. confidence intervals)
- For null hypothesis testing, the test statistic (e.g. F , t , r) with confidence intervals, effect sizes, degrees of freedom and P value noted
Give P values as exact values whenever suitable.
- For Bayesian analysis, information on the choice of priors and Markov chain Monte Carlo settings
- For hierarchical and complex designs, identification of the appropriate level for tests and full reporting of outcomes
- Estimates of effect sizes (e.g. Cohen's d , Pearson's r), indicating how they were calculated

Our web collection on [statistics for biologists](#) contains articles on many of the points above.

Software and code

Policy information about [availability of computer code](#)

Data collection

Live-cell imaging data were collected using METAFLUOR 7.7 or MATscope (available on Github). Fluorimetry data were collected using FlixGX version 4.1.2. 3D organoid imaging data were collected using Nikon software NIS Elements.

Data analysis

Raw imaging data were analyzed using METAFLUOR 7.7, MATLAB (R2021a) (code available on Github) or Nikon software NIS Elements as described in the Methods. Fluorimetry data were analyzed using Microsoft Excel. Statistical analyses were performed using GraphPad Prism 8.

For manuscripts utilizing custom algorithms or software that are central to the research but not yet described in published literature, software must be made available to editors and reviewers. We strongly encourage code deposition in a community repository (e.g. GitHub). See the Nature Portfolio [guidelines for submitting code & software](#) for further information.

Data

Policy information about [availability of data](#)

All manuscripts must include a [data availability statement](#). This statement should provide the following information, where applicable:

- Accession codes, unique identifiers, or web links for publicly available datasets
- A description of any restrictions on data availability
- For clinical datasets or third party data, please ensure that the statement adheres to our [policy](#)

The data that support the findings of this study is available within the main text and its Supplementary Information file. Source data is provided as Source Data file. Data is also available from the corresponding author upon request

Research involving human participants, their data, or biological material

Policy information about studies with [human participants or human data](#). See also policy information about [sex, gender \(identity/presentation\), and sexual orientation](#) and [race, ethnicity and racism](#).

Reporting on sex and gender	N/A
Reporting on race, ethnicity, or other socially relevant groupings	N/A
Population characteristics	N/A
Recruitment	N/A
Ethics oversight	N/A

Note that full information on the approval of the study protocol must also be provided in the manuscript.

Field-specific reporting

Please select the one below that is the best fit for your research. If you are not sure, read the appropriate sections before making your selection.

Life sciences Behavioural & social sciences Ecological, evolutionary & environmental sciences

For a reference copy of the document with all sections, see nature.com/documents/nr-reporting-summary-flat.pdf

Life sciences study design

All studies must disclose on these points even when the disclosure is negative.

Sample size	No statistical methods were used to pre-determine sample sizes. All presented data were from at least triplicates, and replicate numbers were chosen to be sufficient to observe variance, ensure reproducibility, and achieve statistical analysis among groups when required, based on previous work in our group and in the field (e.g. Jinfan Zhang et al. Nat Chem Biol 2021).
Data exclusions	Cells that died or appeared unhealthy during the course of live cell imaging were excluded from analysis. Cells that did not exhibit a stable baseline intensity were excluded from analysis. All exclusion criteria were predetermined.
Replication	Unless otherwise noted, all experiments were repeated at least 3 times. All replication attempts were successful, and number of cells and replicates are indicated in figure legends.
Randomization	Cells were randomly seeded into experimental groups after resuspension. Organoids were randomly seeded with Matrigel into experimental groups after resuspension. Fluorimetry: experimental and control groups were measured before and after ATP treatment with purified PKC α .
Blinding	Blinding was not performed as it was not necessary. Objective quantitative data was generated and analyzed, and no subjective classifications were performed.

Reporting for specific materials, systems and methods

We require information from authors about some types of materials, experimental systems and methods used in many studies. Here, indicate whether each material, system or method listed is relevant to your study. If you are not sure if a list item applies to your research, read the appropriate section before selecting a response.

Materials & experimental systems

n/a	Involved in the study
<input type="checkbox"/>	<input checked="" type="checkbox"/> Antibodies
<input type="checkbox"/>	<input checked="" type="checkbox"/> Eukaryotic cell lines
<input checked="" type="checkbox"/>	<input type="checkbox"/> Palaeontology and archaeology
<input checked="" type="checkbox"/>	<input type="checkbox"/> Animals and other organisms
<input checked="" type="checkbox"/>	<input type="checkbox"/> Clinical data
<input checked="" type="checkbox"/>	<input type="checkbox"/> Dual use research of concern
<input checked="" type="checkbox"/>	<input type="checkbox"/> Plants

Methods

n/a	Involved in the study
<input checked="" type="checkbox"/>	<input type="checkbox"/> ChIP-seq
<input checked="" type="checkbox"/>	<input type="checkbox"/> Flow cytometry
<input checked="" type="checkbox"/>	<input type="checkbox"/> MRI-based neuroimaging

Antibodies

Antibodies used	<p>For Wester Blot, primary antibodies: all antibodies were used at 1:1000 dilution; Mouse anti PKCα (#610108), mouse anti PKCβ (#610128), mouse anti PKCδ (#610397), mouse anti PKCζ (#610175) were from BD Biosciences, mouse anti PKCζ (#17781) was from Santa Cruz Biotechnology and GAPDH (#2118) antibodies from Cell Signaling Technology.</p> <p>For Western blot, secondary antibodies: Horseradish peroxidase-labeled goat anti-rabbit (PI31460) or anti-mouse (PI31430) secondary antibodies were purchased from Pierce</p>
Validation	<p>All antibodies are validated by the suppliers as shown from the links provided below:</p> <p>Mouse anti PKCα (#610108): https://www.bdbiosciences.com/en-us/products/reagents/microscopy-imaging-reagents/immunofluorescence-reagents/purified-mouse-anti-pkc.610108</p> <p>Mouse anti PKCβ (#610128): https://www.bdbiosciences.com/content/dam/bdb/products/global/reagents/western-blotting-and-molecular-reagents/610xxx/6101xx/610128_base/pdf/610128.pdf</p> <p>Mouse anti PKCδ (#610397): https://www.bdbiosciences.com/en-us/products/reagents/microscopy-imaging-reagents/immunofluorescence-reagents/purified-mouse-anti-pkc.610397</p> <p>Mouse anti PKCζ (#610175): https://www.bdbiosciences.com/en-us/products/reagents/microscopy-imaging-reagents/immunofluorescence-reagents/purified-mouse-anti-pkc.610175</p> <p>Mouse anti PKCζ (#17781): https://www.scbt.com/p/pkc-zeta-antibody-h-1</p> <p>Rabbit anti GAPDH (#2118): https://www.cellsignal.com/products/primary-antibodies/gapdh-14c10-rabbit-mab/2118</p> <p>Horseradish peroxidase-labeled goat anti-rabbit (PI31460): https://www.thermofisher.com/antibody/product/Goat-anti-Rabbit-IgG-H-L-Secondary-Antibody-Polyclonal/31460</p> <p>HRP labeled goat anti-mouse (PI31430): https://www.thermofisher.com/antibody/product/Goat-anti-Mouse-IgG-H-L-Secondary-Antibody-Polyclonal/31430</p>

Eukaryotic cell lines

Policy information about [cell lines and Sex and Gender in Research](#)

Cell line source(s)	HEK293T, HeLa, Cos7, MDCK cells were used in this study. All cell lines were obtained from ATCC.
Authentication	Cell line identities were verified via STR analysis by the commercial source and then maintained separately and isolated from one another to avoid cross-contamination.
Mycoplasma contamination	All cell lines were determined to be free of mycoplasma contamination based on weekly DNA staining.
Commonly misidentified lines (See ICLAC register)	No misidentified cell lines were used in this study.

Plants

Seed stocks	<i>Report on the source of all seed stocks or other plant material used. If applicable, state the seed stock centre and catalogue number. If plant specimens were collected from the field, describe the collection location, date and sampling procedures.</i>
Novel plant genotypes	<i>Describe the methods by which all novel plant genotypes were produced. This includes those generated by transgenic approaches, gene editing, chemical/radiation-based mutagenesis and hybridization. For transgenic lines, describe the transformation method, the number of independent lines analyzed and the generation upon which experiments were performed. For gene-edited lines, describe the editor used, the endogenous sequence targeted for editing, the targeting guide RNA sequence (if applicable) and how the editor was applied.</i>
Authentication	<i>Describe any authentication procedures for each seed stock used or novel genotype generated. Describe any experiments used to assess the effect of a mutation and, where applicable, how potential secondary effects (e.g. second site T-DNA insertions, mosaicism, off-target gene editing) were examined.</i>